




Stress-induced vesicular assemblies of dual leucine zipper kinase are signaling hubs involved in kinase activation and neurodegeneration

Elena Tortosa¹ , Arundhati Sengupta Ghosh¹, Qingling Li², Weng Ruh Wong², Trent Hinkle², Wendy Sandoval², Christopher M Rose²  & Casper C Hoogenraad^{1,*} 

Abstract

Mitogen-activated protein kinases (MAPKs) drive key signaling cascades during neuronal survival and degeneration. The localization of kinases to specific subcellular compartments is a critical mechanism to locally control signaling activity and specificity upon stimulation. However, how MAPK signaling components tightly control their localization remains largely unknown. Here, we systematically analyzed the phosphorylation and membrane localization of all MAPKs expressed in dorsal root ganglia (DRG) neurons, under control and stress conditions. We found that MAP3K12/dual leucine zipper kinase (DLK) becomes phosphorylated and palmitoylated, and it is recruited to sphingomyelin-rich vesicles upon stress. Stress-induced DLK vesicle recruitment is essential for kinase activation; blocking DLK-membrane interaction inhibits downstream signaling, while DLK recruitment to ectopic subcellular structures is sufficient to induce kinase activation. We show that the localization of DLK to newly formed vesicles is essential for local signaling. Inhibition of membrane internalization blocks DLK activation and protects against neurodegeneration in DRG neurons. These data establish vesicular assemblies as dynamically regulated platforms for DLK signaling during neuronal stress responses.

Keywords dual leucine zipper kinase; endocytosis; mitogen-activated protein kinase; neurodegeneration; sphingomyelin

Subject Categories Neuroscience; Signal Transduction

DOI 10.15252/emboj.2021110155 | Received 9 November 2021 | Revised 21 April 2022 | Accepted 22 April 2022 | Published online 25 May 2022

The EMBO Journal (2022) 41: e110155

Introduction

Neuronal death is a tightly regulated process, necessary for the proper development of the nervous system and a key pathological event in many neurodegenerative diseases. Elimination of excessive

neurons during the developing nervous system occurs as a failure to establish trophic relationships with a target cell. Neuronal loss becomes highly restricted as the nervous system matures; however, it emerges in response to stroke and traumatic brain injury and contributes to neurodegenerative diseases such as amyotrophic lateral sclerosis and Alzheimer's disease (Mattson, 2000; Yamaguchi & Miura, 2015). Neuronal death is an active and well-orchestrated process with numerous signaling pathways implicated. Among others, mitogen-activated protein kinase (MAPK) signaling pathways have been shown to play key roles in balancing cell survival and death during both development and pathological conditions in numerous cell types including neurons (Kim & Choi, 2010, 2015). Despite the critical importance of MAPK cascades, it remains largely unknown how MAPKs signaling is spatially and temporally controlled in complex neuronal cells under the various stress conditions.

Different MAPK cascades have been reported to differentially contribute to neuronal survival and degeneration. For example, it is widely accepted that MAPKs such as c-Jun N-terminal kinase (JNK) and p38 MAPK (p38) promote cell death, whereas extracellular signal-regulated kinase 1/2 (ERK1/2) contribute to neuron survival (Xia *et al.*, 1995; Hetman & Gosh, 2004; Yarza *et al.*, 2016; Asih *et al.*, 2020). MAP3Ks have been shown to function as critical nodes in neuronal signaling pathways. For instance, MAP3K12/ dual leucine zipper kinase (DLK) mediates neuronal death induced by nerve growth factor (NGF) deprivation in sympathetic neurons, and DLK, together with leucine zipper-bearing kinase (LZK), MAPK/ERK kinase 4 (MEKK4), and mixed lineage kinase 2 (MLK2), are key mediators of cell death in response to traumatic injury (Ghosh *et al.*, 2011; Yang *et al.*, 2015). Interestingly, pharmacological and genetic inhibition of MAP3Ks such as DLK and LZK are sufficient to attenuate neuronal death in different models of acute neuronal injury and neurodegenerative diseases (Chen *et al.*, 2008; Miller *et al.*, 2009; Ghosh *et al.*, 2011; Pozniak *et al.*, 2013; Watkins *et al.*, 2013; Fernandes *et al.*, 2014; Patel *et al.*, 2015; Le Pichon *et al.*, 2017; Welsbie *et al.*, 2013; Welsbie *et al.*, 2017; Welsbie *et al.*, 2019; Wlaschin *et al.*, 2018; Hu *et al.*, 2019; Ma *et al.*, 2021).

¹ Department of Neuroscience, Genentech, Inc., South San Francisco, CA, USA

² Department of Microchemistry, Proteomics and Lipidomics, Genentech, Inc., South San Francisco, CA, USA

*Corresponding author (Lead contact). Tel: +1 650 467 2877; E-mail: hoogenraad.casper@gene.com

Considering the broad range of stimuli that activate MAPK signaling cascades and the large number of processes that these kinases regulate, MAPK specificity needs to be tightly controlled. A precise and dynamic subcellular localization of the MAPK cascade components is critical to tightly control kinase (in)activation and the access to downstream effectors (Witzel *et al*, 2012; Wainstein & Seger, 2016; Zhang *et al*, 2021). The mechanisms that control kinase localization are not fully understood but may include interactions with specific adaptor proteins or lipids. For example, in resting conditions, specific anchor proteins retain components of the Raf-MEK-ERK cascade such as ERK1/2 in the cytoplasm in different cell lines (Fukuda *et al*, 1997; Brunet *et al*, 1999; Formstecher *et al*, 2001; Chen *et al*, 2005; Mebratu *et al*, 2008). Upon stimulation, the components of the cascade rapidly change their subcellular location: Rafs are known to move to the plasma membranes and other intracellular membranes, whereas active MEK1/2 and ERK1/2 translocate from the cytosol to the nucleus in numerous cell types including neurons (Eblen, 2018). In addition, lipid modifications such as palmitoylation have been shown to target MAPKs such as DLK and JNK3 to membranes, controlling not only localization and activity but also protein stability in neurons (Yang *et al*, 2012; Holland *et al*, 2016; Niu *et al*, 2022). Understanding the complex subcellular localization of MAPK cascade components in neurons and their dynamic changes upon stress will provide a better understanding of the regulation of signaling pathways involved in neuronal survival and degeneration.

Here, we systematically analyze changes in phosphorylation and localization of MAPKs expressed in dorsal root ganglia (DRG) neurons, in control and stress conditions. MAPKs such as c-Raf, MEKK2, and ERK1/2 decrease their phosphorylation levels in response to NGF deprivation. Interestingly, DLK is the only MAPK that responds by increasing its phosphorylation and membrane localization. NGF deprivation-induced stress also promotes DLK palmitoylation which changes its localization from the cytoplasm to axonal transport vesicles. Preventing DLK vesicle assembly inhibits DLK-mediated signaling pathways, and conversely, ectopic recruitment of DLK to other subcellular structures is sufficient to induce its activation. We show that DLK vesicle recruitment is independent of DLK dimerization or kinase activation, but relies on an active

endocytic pathway and sphingomyelin levels in the neuron. These findings provide new insights into the mechanism of DLK activation in neurons and suggest that stress-induced DLK vesicle assemblies act as local signaling platforms that drive kinase activation and neurodegeneration.

Results

Neuronal stress increases DLK recruitment to membranes

MAPK cascades respond to various stimuli and control both survival and apoptosis signaling. The subcellular localization of MAPK components has been shown to be key in controlling their activity and specificity. We decided to systematically characterize the different MAPK family members and their membrane localization during neuronal stress using an *in vitro* model that mimics the competition for trophic factors experienced by sensory neurons *in vivo*. Cultured DRG neurons *in vitro* require the presence of NGF to survive, and NGF depletion initiate an active and tightly controlled process of degeneration (Deshmukh & Johnson, 1997; Freeman *et al*, 2004). Interestingly, the molecular machinery involved in this developmental neurodegeneration process is activated in adult axonal injury and various neurodegenerative diseases (Asghari Adib *et al*, 2018). We first analyzed total protein expression and phosphorylation of the different MAPK cascade components by mass spectrometry. Many different MAPKs were expressed in DRG primary cultures, including MAPK, MAP2K, and MAP3K members (Fig 1A). Although none of the MAPK family member changed their expression at total protein levels (Dataset EV1), some of them, such as DLK, ERK1/2, MEKK2, and c-Raf, altered their phosphorylation levels after 1 and 4 h of NGF deprivation (Fig 1B, Appendix Fig S1A). In addition to the changes in DLK phosphorylation, we also found increased phosphorylation levels of the downstream effector c-Jun after NGF deprivation, but could not detect sustained changes in phosphorylation levels of intermediate kinases such as JNK1/2/3 or MKK4/7 during the 4-h time window in this particular mass spectrometry experiment (Dataset EV1). We next tested the membrane association of the different MAPKs present in

Figure 1. Neuronal stress increases DLK recruitment to membranes.

- Schematic diagram of MAPK signaling cascades in mammalian cells. Only representative signaling molecules are shown. MAPK cascade components detected in 3 days *in vitro* (DIV) cultured embryonic DRG neurons by TMT-based mass spectrometry analysis are colored. In grey, MAPKs not detected ($n = 2$ independent experiments).
- Volcano plot of differently-regulated phosphosites of MAPK cascade components from 3DIV cultured embryonic DRG neurons upon 4 h of NGF deprivation, with protein-level cut-offs set at \log_2 fold change > 1.0 and $-\log_{10}$ adjusted P -value > 1.3 ($P < 0.05$), marked by dashed lines. Downregulated sites represented as blue points, and up-regulated sites as orange points ($n = 2$ independent experiments).
- Representative Western blots of the different MAPKs expressed in DRG neurons (DIV3) cultured in the presence or absence of NGF for 3 h and subjected to a membrane/cytosolic fractionation. α -tubulin and STMN-1 are used as controls of cytosolic proteins and Na^+/K^+ -ATPase and STMN-2 as controls of membrane proteins.
- Quantification of the ratio of protein localized in the membrane fraction after 3 h of NGF deprivation ($n = 6$ –14 biological replicates; series of unpaired t -tests followed by a Holm-Sidak correction).
- Flow chart showing the approach used to detect palmitoylation levels in DLK from cultured embryonic DRG neurons. Palmitoylated proteins were labeled with click-it palmitic acid, conjugated with biotin and subjected to immunoprecipitation using streptavidin beads.
- Representative Western blots of total and palmitoylated DLK (upper panel) and quantification of DLK palmitoylation levels (lower panel) from cultured DRG neurons subjected to 3 h of NGF deprivation ($n = 5$ independent experiments; Mann-Whitney U test).

Data information: Graphs represent mean \pm SEM in (D) and (F). * $P < 0.05$ and ** $P < 0.01$. Diagrams in A and E were created with BioRender.com. See also Appendix Fig S1.

Source data are available online for this figure.

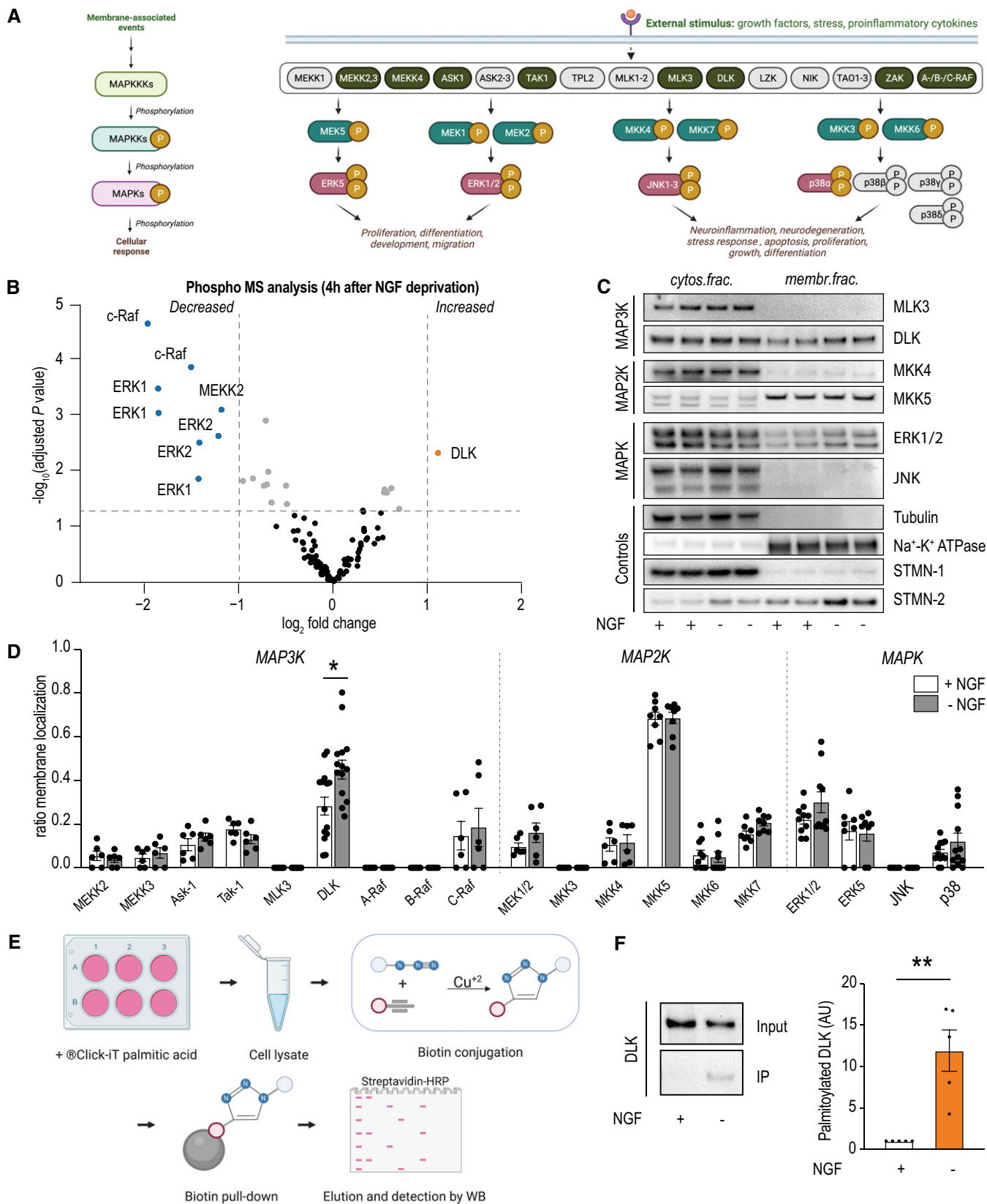


Figure 1.

DRG neurons and determined whether their localization was altered upon NGF deprivation. By performing membrane fractionation experiments of DRG neurons after NGF withdrawal, we found that kinases such as DLK, MKK5, or ERK1/2 partially or fully coincided with membranes. However, only DLK changed its membrane association upon NGF withdrawal (Fig 1C and D, Appendix Fig S1B). Membrane anchoring of cytosolic protein can be mediated by palmitoylation (Iwanaga *et al*, 2009). We confirmed that several MAPK can be palmitoylated in DRG neurons using click-it chemistry (Fig 1E, Appendix Fig S1C) and observed that, in agreement with the stress-induced membrane recruitment, DLK increased its palmitoylation levels upon NGF deprivation while total protein levels remained unchanged (Fig 1F, Appendix Fig S1D). These findings are in line with previous studies in which DLK was described to respond to cellular stress (Tedeschi & Bradke, 2013; Asghari Adib *et al*, 2018). As DLK is the only MAPK in DRG neurons that responded by increasing its protein phosphorylation and membrane association, we decided to further characterize the role of DLK-membrane associations and its impact on DLK activity and neurodegeneration.

DLK vesicle recruitment induces kinase activation and signaling upon stress

We next analyzed the subcellular localization of DLK under control and stress induced by NGF deprivation. Using live imaging experiments in DRG neurons, we found that GFP-tagged DLK was present in vesicle-like structures that were transported along the axon, in both anterograde and retrograde directions (Fig 2A and B). Similar vesicle localization was observed for endogenous DLK (Fig 2C, Appendix Fig S2A). DLK localization was prevented by the

pharmacological inhibitor of protein palmitoylation, 2-bromopalmitate (2-BP) or by point mutation of DLK's palmitoylation site, Cys-127 (Appendix Fig S2B and C) (Holland *et al*, 2016). We observed an increase in the number of DLK-positive vesicles after NGF withdrawal for both endogenous and overexpressed GFP-tagged DLK in DRG neurons (Fig 2D–G), consistent with the increase in membrane association in the fractionation experiments.

To further explore the role of vesicle recruitment during DLK signaling, we next tested whether displacing DLK from vesicles could block DLK activity. We overexpressed an N-terminal portion of DLK (1–162 aa) including the palmitoylation region but without the kinase domain, and analyzed the levels of p-c-Jun as a readout of endogenous DLK activation. We observed that the N-terminal domain is recruited to vesicles and reduces the activation of DLK in response to NGF withdrawal (Fig 2H–J). To further determine the importance of DLK recruitment for the kinase activity, we measured the activity of DLK upon recruitment to ectopic membrane of structures such as the endoplasmic reticulum, the plasma membrane, or mitochondria using the transmembrane domain of VAPB (DLK-WT-ER), the C-terminal CAAX motif of Ras proteins (DLK-WT-CAAX) or the membrane targeting sequence of the ActA protein of *Listeria monocytogenes* (DLK-WT-MTS), respectively (Fig 2K). We observed that upon intracellular membrane recruitment to structures such as the endoplasmic reticulum or mitochondria DLK increases the phosphorylation of c-Jun, indicating that recruiting DLK to ectopic subcellular structures is sufficient to induce kinase activation. To exclude the possibility of an additional recruitment of DLK to Golgi membranes, we tested the activity of the C127S palmitoyl mutant DLK (DLK-CS) ectopically recruited to similar structures. As observed before, palmitoyl mutant DLK is activated when recruited to structures such as endoplasmic reticulum or mitochondria (Fig 2L–N, Appendix Fig S2D and E). Together, these

Figure 2. DLK vesicle recruitment induces kinase activation and signaling upon stress.

- A Representative stills from time-lapse recordings of DIV6 DRG neurons overexpressing DLK-GFP. Arrowheads point to individual moving DLK-GFP positive structures.
- B Kymographs made from the complete time-lapse recording shown in A. The left shows the original kymograph, and the right shows an illustration of the manually traced structure displacements for better visualization.
- C Representative images of DIV3 DRG neurons nucleofected with a non-targeting siRNA (NT siRNA) or a siRNA against DLK (DLK siRNA), and stained for endogenous DLK and β -tubulin (TUBB3). On the right, quantification of the DLK mean intensity in neurons expressing control NT or DLK siRNAs ($n = 25$ neurons/condition; Unpaired *t*-test).
- D–F Representative kymographs (D), quantification of GFP-positive particle number (E) and percentage of anterograde, retrograde, reverse or non-moving GFP-positive particles (F) from DLK-GFP time-lapse recordings in DIV6 DRG neurons, in control situation (+NGF) or after 3 h of NGF deprivation (–NGF) ($n = 45$ –46 neurons/condition; Mann–Whitney *U* test in E and Chi-square test in F).
- G Representative images of DIV3 cultured embryonic DRG neurons maintained in the presence (+NGF) or absence (–NGF) of NGF for 3 h and stained for endogenous DLK. On the right, quantification of the number of DLK-positive puncta in control situation or after 3 h of NGF deprivation ($n = 18$ –19 neurons/condition; Mann–Whitney *U* test).
- H Representative kymograph and stills from a time lapse recording of 6DIV neurons overexpressing a GFP-tagged N-terminal region of DLK (NtermDLK-GFP). Arrowheads point to individual moving NtermDLK-GFP positive structures.
- I, J Representative Western blots of p-cJun and GAPDH (I), and quantification of relative c-Jun phosphorylation levels (J) from DIV6 cultured embryonic DRG neurons overexpressing GFP or NtermDLK-GFP, and subjected to NGF withdrawal for 3 h ($n = 7$ –8 biological replicates; series of unpaired *t*-tests /Mann–Whitney *U* tests followed by a Holm–Sidak correction).
- K Diagram of different DLK constructs fused with the transmembrane domain of VAPB (DLK-ER), the C-terminal CAAX motif of Ras proteins (DLK-CAAX) or the membrane targeting sequence of the ActA protein of *Listeria monocytogenes* (DLK-MTS), and their expected localization.
- L Representative images of HeLa cells expressing the different HA-tagged wild-type (WT) and palmitoyl-mutant (CS) DLK constructs (DLK-WT-ER, DLK-CS-ER, DLK-WT-CAAX, DLK-CS-CAAX, DLK-WT-MTS, DLK-CS-MTS), and stained with markers of the endoplasmic reticulum (KDEL), plasma membrane (CellMask) and mitochondria (cytochrome C).
- M, N Representative Western blots of DLK, p-cJun and GAPDH (M) and quantification of relative c-Jun phosphorylation levels (N) from HeLa cells transfected with HA alone (HA) and the different HA-tagged wild-type (WT) and palmitoyl-mutant (CS) DLK constructs (DLK-WT-ER, DLK-CS-ER, DLK-WT-CAAX, DLK-CS-CAAX, DLK-WT-MTS, DLK-CS-MTS) ($n = 7$ –8 biological replicates; series of unpaired *t*-tests /Mann–Whitney *U* tests with DLK-WT or DLK-CS followed by a Holm–Sidak correction).
- Data information: All graphs represent mean \pm SEM. * $P < 0.05$ ** $P < 0.01$ and *** $P < 0.001$. Scale bar represents 10 μ m in (B) and (C), 5 μ m in (A), (D), (G), (H) and (L), and 2 μ m in zooms in (C). See also Figure Appendix Fig S2.
- Source data are available online for this figure.

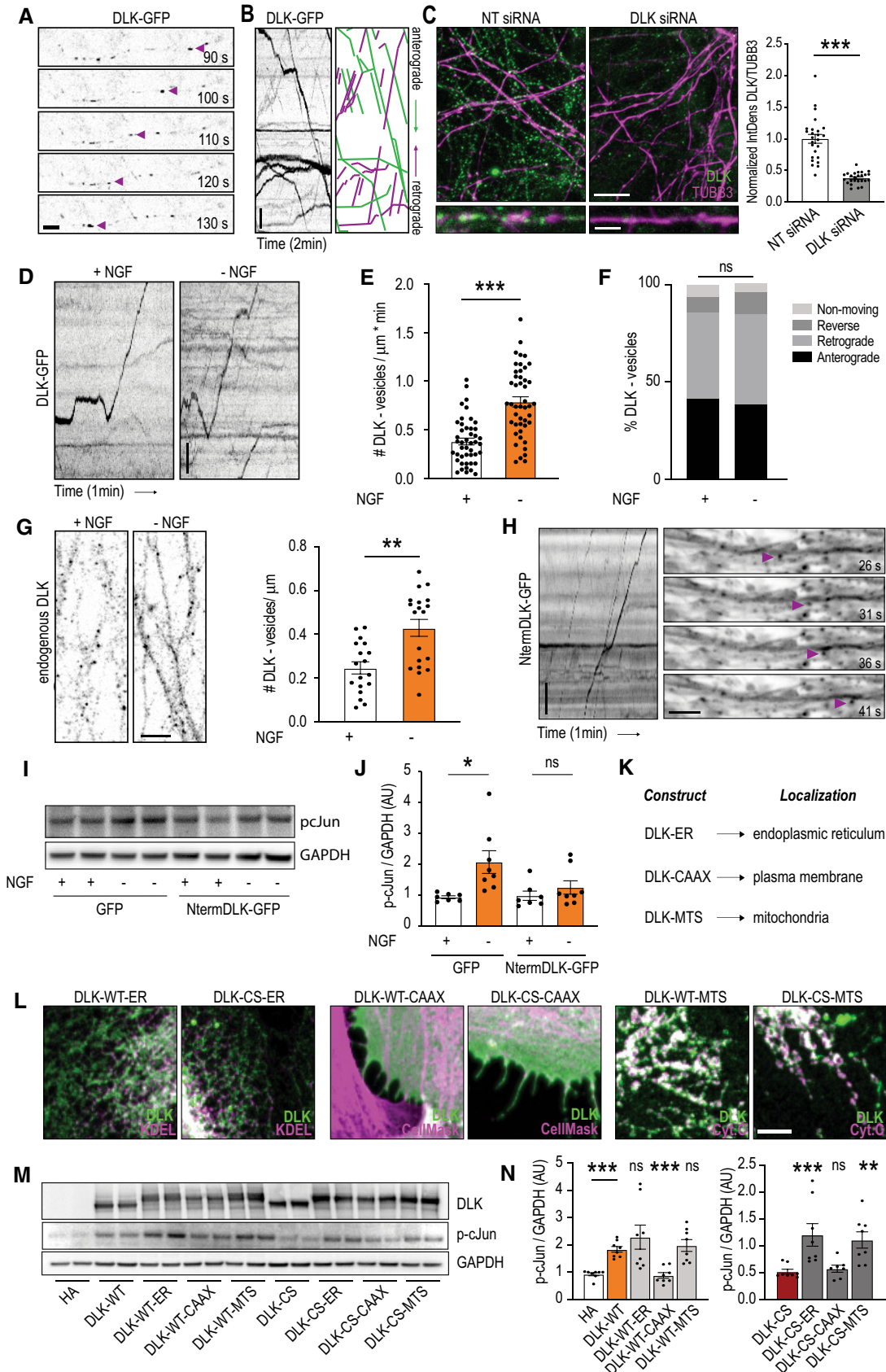


Figure 2.

data suggest that DLK vesicle localization is critical for the kinase activation and downstream signaling in response to stress.

DLK-vesicle localization is independent of its activation state

To further elucidate whether DLK vesicle recruitment requires dimerization and kinase activity, we generated a series of point mutations in the kinase and leucine zipper domains of DLK, DLK-KD-GFP, and DLK-LZ-GFP, respectively (Fig 3A, Appendix Fig S2F). It has been shown that DLK overexpression is sufficient for DLK activation and phosphorylation of c-Jun in cell lines (Mata *et al*, 1996). We expressed the mutant constructs in HeLa cells and found that, with the exception of the GFP-tagged wild-type DLK (DLK-WT-GFP), all mutated constructs were inactive and did not increase the phosphorylation levels of c-Jun (Fig 3B and C). We next analyzed the localization of the different mutants and found that DLK-WT-GFP was present at intracellular vesicles. The vesicular association was dependent on palmitoylation because the palmitoyl mutant (DLK-CS-GFP) shifted DLK to a cytoplasmic localization. Interestingly, both DLK-KD-GFP and DLK-LZ-GFP also showed a punctate localization (Fig 3D). Consistently, subcellular fractionations showed that all constructs tested were equally present in both membrane and cytosolic compartments, with the exception of DLK-CS-GFP, that was highly enriched in the cytosolic fraction (Fig 3E and F). We next performed similar experiments in DRG neurons and found that, consistently with results obtained in HeLa cells, all DLK mutants were recruited to vesicles, with the exception of DLK-CS (Fig 3G–I). In agreement with these data, treatments with DLK inhibitor (GNE-3511) did not block DLK vesicle localization. Interestingly, DLK inhibitor increased the number of DLK-positive vesicles in DRG neurons (Fig 3J–L). These results demonstrate that DLK vesicle localization is dependent on protein palmitoylation but is independent of protein dimerization or kinase activity.

Sphingomyelin regulates DLK-vesicle localization and kinase activity

We next determined the identity of the DLK-positive vesicles by staining for various vesicular structures, including markers for the

secretory pathway, such as post-Golgi secretory vesicles (Rab6) and synaptic precursor vesicles (Rab3), and markers for vesicles from the endocytic pathway, including late endosomes (Rab7) and recycling endosomes (Rab11) (Fig 4A). Object-based colocalization analysis revealed that DLK was present on various vesicles in the secretory and endosomal pathway, and was not associated with a specific vesicular subcompartment (Fig 4B, Appendix Fig S3A–C). Based on these results, we investigated whether DLK-positive vesicles have a unique lipid signature. We expressed control HA, DLK-WT-HA, and DLK-CS-HA in HeLa cells, performed anti-HA pull downs, and ran an unbiased lipidomic analysis on the samples. We found that vesicles containing overexpressed HA-tagged DLK were enriched in lipids such as phosphatidylethanolamine, phosphatidylcholines, and sphingomyelin (Fig 4C–E). From these lipids only sphingomyelin levels and species were significantly different between DLK-WT-HA and DLK-CS-HA (Fig 4E and F). Consistently, inhibition of sphingomyelin synthase with compounds such as D609 blocked both DLK-vesicle localization and the increase in c-Jun phosphorylation induced by NGF withdrawal, while did not affect vesicular structures, axon integrity and neuron viability (Fig 4G–L, Appendix Fig S3D–G). Together, the data suggest that DLK vesicle localization and further kinase activation requires the presence of sphingomyelin in membrane vesicles.

Endocytosis is required for DLK-vesicle localization and signaling

Sphingomyelin is synthesized at the endoplasmic reticulum and Golgi apparatus, and is present in both the endocytic and the secretory pathway (Gault *et al*, 2010; Yang *et al*, 2018). As DLK-membrane localization depends on sphingomyelin and DLK is found on both endocytic and secretory vesicles, we next investigated which vesicular trafficking pathway is involved in DLK signaling. We first performed treatments with either brefeldin-A to disrupt the secretory pathway and the dynamin inhibitor dynasore to block dynamin-dependent endocytosis, in DRG neurons under control and NGF deprivation. We immunoblotted for p-c-Jun as a readout of DLK activation and found that, whereas brefeldin-A did not affect levels of c-Jun phosphorylation, treatments with dynasore completely abolished the increase in phosphorylation of c-Jun under

Figure 3. DLK-vesicle localization is independent of its activation state.

- A Schematic diagram of DLK indicating point mutations generated for the different GFP-tagged DLK constructs.
- B, C Representative Western blots of GFP, p-cJun and GAPDH (B) and quantification of relative c-Jun phosphorylation levels (C) from HeLa cells non transfected (NT) or transfected with GFP alone (GFP), GFP-tagged DLK wild-type (DLK-WT-GFP), kinase dead mutant (DLK-KD-GFP), leucine zipper domain mutant (DLK-LZ-GFP) and a palmitoyl-site mutant (DLK-CS-GFP) ($n = 4-7$ biological replicates; series of unpaired *t*-tests /Mann-Whitney *U* tests with DLK-WT-GFP followed by a Holm-Sidak correction).
- D Representative images and zooms of HeLa cells expressing GFP alone or the different GFP-tagged DLK mutants.
- E, F Representative Western blots of GFP, α -tubulin and Na^+/K^+ -ATPase from cytosolic and membrane fractions (E) and quantification of the percentage of DLK localized in the membrane and cytosolic fraction (F) from HeLa cells expressing GFP alone or the different GFP-tagged DLK mutants ($n = 4-5$ biological replicates; series of unpaired *t*-tests /Mann-Whitney *U* tests with DLK-WT-GFP followed by a Holm-Sidak correction).
- G–I Representative stills (G), representative kymographs (H) and quantification of the number of GFP-positive particles (I) from time-lapse recordings of the different GFP-tagged DLK mutants in DIV6 cultured embryonic DRG neurons ($n = 31-65$ neurons/condition; series of Mann-Whitney *U* tests with DLK-WT-GFP followed by a Holm-Sidak correction).
- J–L Representative stills (J), kymographs (K) and quantification of the number of DLK-GFP positive particles (L) from time-lapse recordings of DIV6 DRG neurons overexpressing GFP-tagged DLK and treated with control (DMSO) or DLK inhibitor GNE-3511 (DLKi) for 3 h ($n = 22-46$ neurons/condition; Unpaired *t*-test).

Data information: Arrowheads point to individual DLK-GFP positive structures in G and J. All graphs represent mean \pm SEM. * $P < 0.05$ and *** $P < 0.001$. Scale bar represents 100 μm in (D), 10 μm in (G) and (J), 5 μm in (H), (K) and zooms in (D). See also Appendix Fig S2.

Source data are available online for this figure.

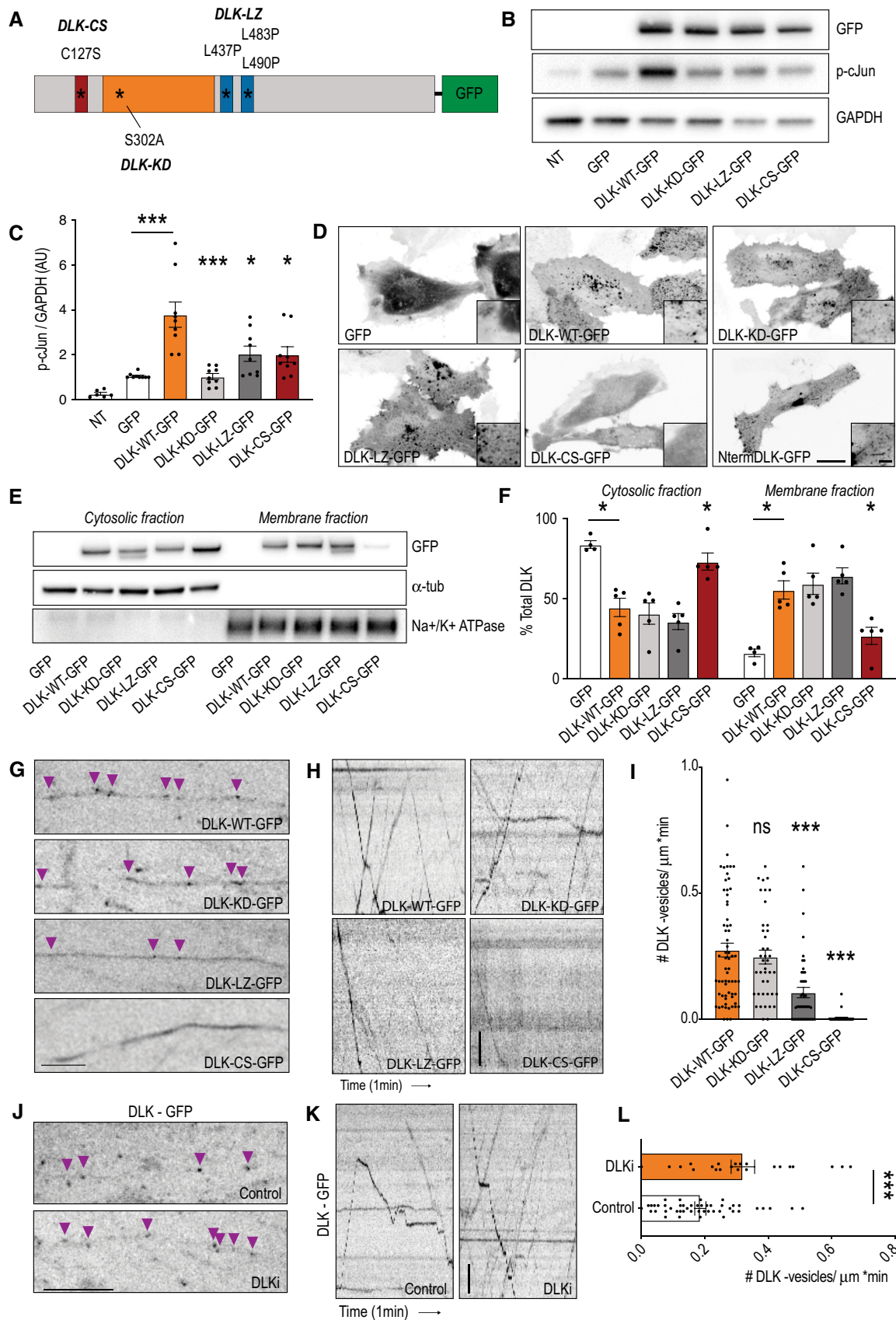


Figure 3.

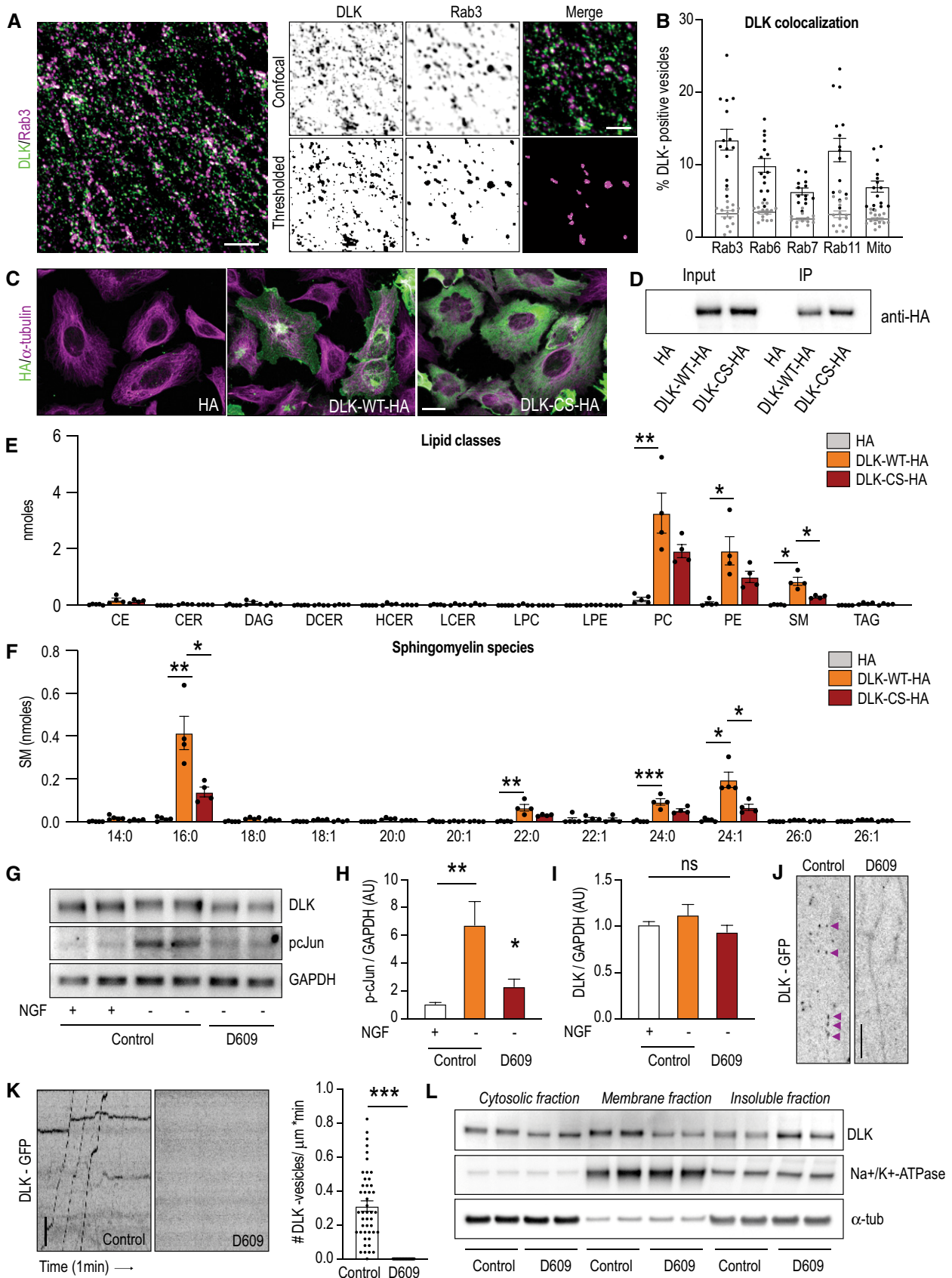


Figure 4.

Figure 4. Sphingomyelin controls DLK—vesicle localization and kinase activity.

- A Representative confocal deconvolved and thresholded images of DIV3 cultured embryonic DRG neurons co-stained for endogenous DLK (green) and the marker for synaptic vesicles Rab3 (magenta).
- B Colocalization analysis between DLK (black values) or same image after 90° rotation (grey values), and markers for different intracellular compartments (Rab3, Rab6, Rab7, Rab11 and mitochondria) in DIV3 cultured embryonic DRG neurons ($n = 13–17$ images/condition).
- C Representative images of HeLa cells expressing HA alone and the different HA-tagged DLK constructs: a wild-type form of DLK (DLK-WT-HA) and the palmitoyl-mutant DLK (DLK-CS-HA).
- D Western blot analysis from total lysate (Input) and immunoprecipitates (IP) of HA-tag protein immunoprecipitations in HeLa cells overexpressing HA alone and the different HA-tagged DLK constructs, DLK-WT-HA and DLK-CS-HA in the absence of any detergent.
- E, F Lipidomic analysis of the immunoprecipitates obtained from the HA-tagged protein immunoprecipitations from extracts of HeLa cells overexpressing HA alone, DLK-WT-HA and DLK-CS-HA. Quantification of lipid classes (E) and sphingomyelin fatty acid species (F) measured in the immunoprecipitates ($n = 3–4$ independent experiments; series of unpaired t -tests /Mann–Whitney U tests followed by a Holm–Sidak correction).
- G–I Representative Western blots of DLK, p-cJun and GAPDH (G) and quantification of relative c-Jun phosphorylation (H) and DLK levels (I) from 3DIV cultured embryonic DRG neurons treated with D609 for 3 h in the presence or absence of NGF ($n = 8$ biological replicates; series of unpaired t -tests with control NGF withdrawal condition followed by a Holm–Sidak correction).
- J, K Representative stills (J), kymographs and quantification of the number of DLK-GFP positive particles (K) from time-lapse recordings from 6DIV cultured embryonic DRG neurons overexpressing GFP-tagged DLK and treated with D609 for 3 h ($n = 29–46$ neurons; Mann–Whitney U test). Arrowheads in J point to individual DLK-GFP positive structures.
- L Representative Western blots of DLK, α -tubulin and Na^+/K^+ -ATPase from cytosolic, membrane and insoluble fractions of 3DIV cultured embryonic DRG neurons treated with D609 for 3 h.

Data information: All graphs represent mean \pm SEM. * $P < 0.05$ ** $P < 0.01$ and *** $P < 0.001$. CE, cholesteryl ester; CER, ceramide; DAG, diacylglycerol; DCER, dihydroceramides; HCEr, hexosylceramides, LCEr, lactosylceramides; LPC, lysophosphatidylcholine; LPE, lysophosphatidylethanolamine; PC, phosphatidylcholine; PE, phosphatidylethanolamine; SM, sphingomyelin; TAG, triacylglycerol. Scale bar represents 20 μm in (C), 10 μm in (J), 5 μm in (A) and (K), and 2 μm in zooms in (A). See also Figure Appendix Fig S3.

Source data are available online for this figure.

NGF withdrawal (Fig 5A). Consistently, dynasore treatments blocked the increase in phosphorylation of the downstream effector MKK4 whereas did not affect compartments such as mitochondria or axon integrity (Hirai *et al*, 1997; Xu *et al*, 2001; Huntwork-Rodriguez *et al*, 2013) (Fig 5B, Appendix Fig S3H–J). We next analyzed the DLK localization in DRG neurons and observed that brefeldin-A treatments did not change DLK vesicle localization whereas dynasore completely abolished DLK vesicle recruitment (Fig 5C–F). Consistently, dynasore treatments blocked DLK membrane recruitment observed by fractionation experiments after NGF withdrawal (Fig 5G and H). We next tested other endocytosis inhibitors in these assays: hypertonic sucrose media (HS), chlorpromazine (CHP), and dansylcadaverine (DCV) as inhibitors of clathrin-dependent endocytosis, and methyl- β -cyclodextrin (MCD) as an inhibitor of clathrin-independent and caveolin-dependent endocytosis pathway. We found that inhibition of either pathway was sufficient to block DLK vesicle localization and activation after NGF withdrawal (Fig 5I–L, Appendix Fig S3K and L). Interestingly, dynasore not only blocked NGF withdrawal dependent signaling but also inhibited DLK activation by a different stressor such as vincristine (Fig 5M). These data suggest that membrane internalization, both clathrin-dependent and -independent are required for DLK-vesicle localization and signaling upon various neuronal stressors.

Inhibition of endocytosis protects against axon degeneration and neuronal apoptosis

Given the essential role of DLK-vesicle recruitment for DLK-dependent downstream signaling and the robust effects of dynasore on DLK localization and activity, we next assessed whether membrane internalization is required for apoptotic pathway activation and further axon degeneration. To test whether the effect of endocytosis inhibition similarly blocked neuronal apoptosis, we immunoblotted for activated caspase-3. Treatments with dynasore

reduced the levels of activated caspase-3 8 h after NGF withdrawal (Fig 6A). Consistently, similar effects were observed with inhibitors of clathrin-dependent and -independent endocytosis and by overexpressing a dominant negative form of dynamin-1 (Fig 6B and C). To determine whether treatments with dynasore were sufficient to attenuate axonal degeneration in DRG neurons after NGF deprivation, we treated DRG explants and dissociated DRG neurons with different concentrations of dynasore. Examination of DRG explants after 24 h of NGF withdrawal showed a robust protective effect of dynasore treatments on axon degeneration while neuron viability was not affected (Fig 6D, Appendix Fig S4A and B). Similar axon protective effects were observed in dissociated DRG neurons in a dose-response relationship and by overexpressing a dominant-negative form of dynamin-1 (Fig 6E and F, Appendix Fig S4C), suggesting that membrane internalization acts as a key upstream regulator of the DLK signaling pathway. Together, these data show that inhibition of endocytosis protects neurons from DLK activation and subsequent apoptotic signaling and axon degeneration.

Discussion

MAPK signaling during neuronal cell death

Growth factors such as NGF mediate neuronal survival and NGF withdrawal from cultured embryonic DRG neurons have been shown to initiate an acute stress response that shares several aspects with adult axonal injury responses (Kristiansen & Ham, 2014). The induction of neuronal death by NGF deprivation involves the activation of a robust MAPK signaling system of which many factors remain unknown. Here, we systematically analyze changes in protein levels, phosphorylation and membrane localization of MAPKs expressed in DRG cultured neurons in response to NGF withdrawal. Consistent with previous studies

reporting no changes in MAPKs mRNA following NGF deprivation (Maor-Nof et al, 2016; Larhammar et al, 2017), we observe no major changes in MAPK protein expression. We also analyzed protein phosphorylation by mass spectrometry and found that NGF

deprivation decreases phosphorylation levels of MAPKs such as c-Raf and ERK1/2, and increases phosphorylation of DLK. These data agree with previous reports describing an inhibition of the Raf-MEK-ERK cascade and a stimulation of the JNK signaling

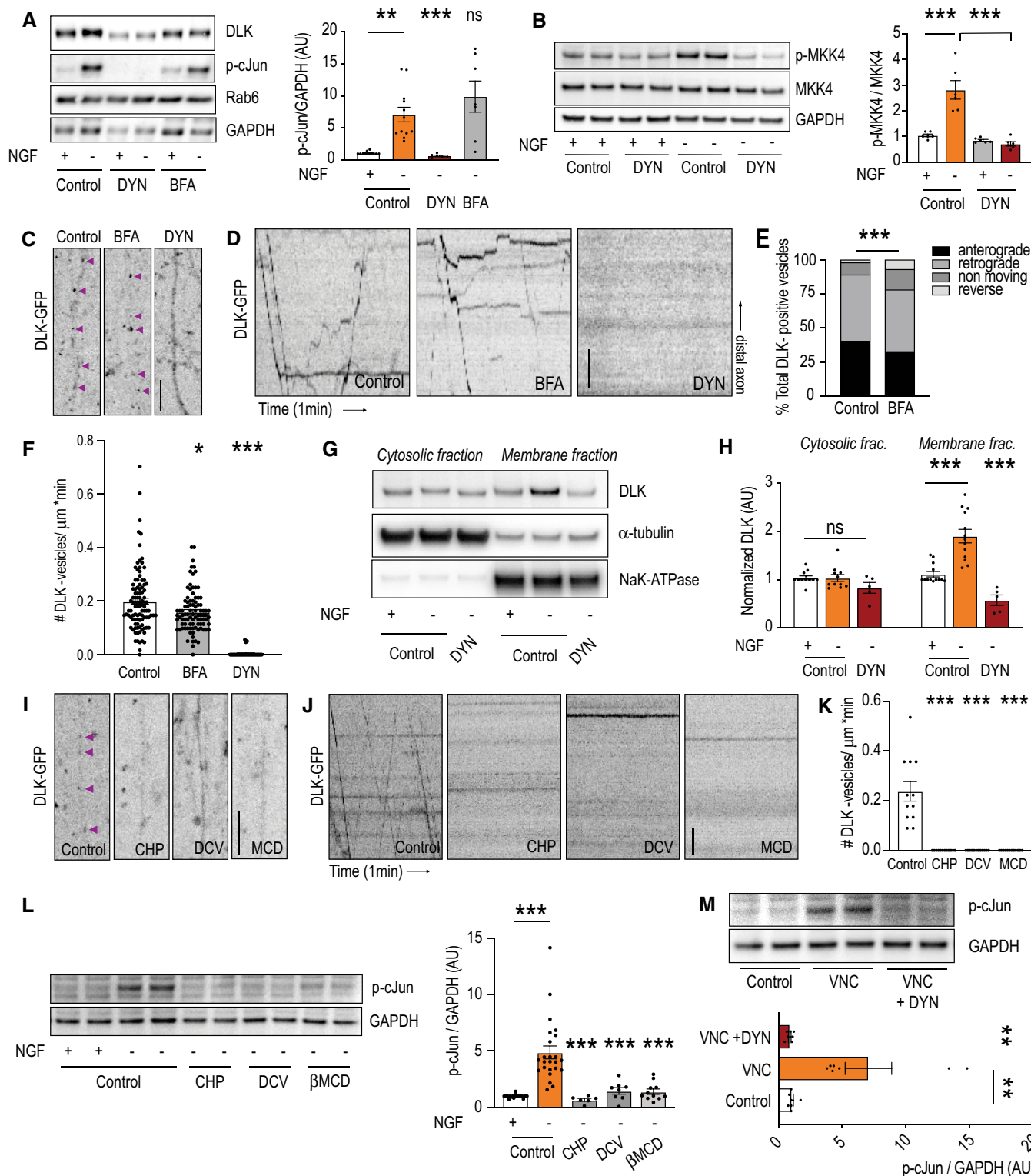


Figure 5.

Figure 5. DLK uses the endocytic pathway as a platform for signaling.

- A Western blot analysis of endogenous DLK, p-cJun, Rab6 and GAPDH, and quantification of relative c-Jun phosphorylation levels in 3DIV cultured embryonic DRG neurons treated with dynasore (DYN) or brefeldin A (BFA) for 3 h in the presence or absence of NGF ($n = 6$ –12 biological replicates; series of unpaired *t*-tests / Mann–Whitney *U* tests with control NGF withdrawal followed by a Holm–Sidak correction).
- B Representative Western blots of p-MKK4, MKK4 and GAPDH, and quantifications of the relative MKK4 phosphorylation levels in 3DIV cultured embryonic DRG neurons treated with dynasore (DYN) for 3 h in the presence or absence of NGF ($n = 6$ biological replicates, series of unpaired *t*-tests with control NGF withdrawal followed by a Holm–Sidak correction).
- C–F Representative stills (C), kymographs (D) and quantification of the orientation (E) and number of DLK-GFP positive particles (F) from time-lapse recordings of DIV6 DRG neurons overexpressing GFP-tagged DLK and treated with dynasore (DYN) or brefeldin A (BFA) for 3 h ($n = 34$ –101 neurons, Chi-square test in E and series of Mann–Whitney tests with control followed by a Holm–Sidak correction in F). Arrowheads in C point to individual DLK-GFP positive structures.
- G, H Representative Western blots of DLK, α -tubulin and Na⁺/K⁺-ATPase (G) and quantifications (H) from cytosolic and membrane fractions of 3DIV cultured embryonic DRG neurons treated with dynasore (DYN) for 3 h in the absence of NGF ($n = 5$ –11 biological replicates, series of unpaired *t*-tests / Mann–Whitney *U* tests with control NGF withdrawal followed by a Holm–Sidak correction).
- I–K Representative stills (I), kymographs (J) and quantification of the number of DLK-GFP positive particles (K) from cultured embryonic DRG neurons treated with chlorpromazine (CHP), dansylcadaverine (DCV) or methyl- β -cyclodextrin (MCD) for 3 h ($n = 12$ neurons, series of Mann–Whitney *U* tests with control situation followed by a Holm–Sidak correction). Arrowheads in I point to individual DLK-GFP positive structures.
- L Representative Western blots of p-cJun and GAPDH, and quantification of relative c-Jun phosphorylation levels in 3DIV cultured embryonic DRG neurons treated with chlorpromazine (CHP), dansylcadaverine (DCV) or methyl- β -cyclodextrin (MCD) for 3 h in the absence of NGF ($n = 6$ –24 biological replicates, series of Mann–Whitney *U* tests with control NGF withdrawal followed by a Holm–Sidak correction).
- M Representative Western blots of p-cJun and GAPDH, and quantification of relative c-Jun phosphorylation levels in 3DIV cultured embryonic DRG neurons treated with vincristine (VNC) and dynasore (DYN) for 3 h ($n = 7$ biological replicates, series of Mann–Whitney *U* tests with vincristine condition followed by a Holm–Sidak correction).

Data information: All graphs represent mean \pm SEM. * $P < 0.05$ ** $P < 0.01$ and *** $P < 0.001$. Scale bar represents 10 μ m in (C) and (I), 5 μ m in (D) and (J). See also Figure Appendix Fig S3.

Source data are available online for this figure.

pathway upon NGF withdrawal (Virdee & Tolkovsky, 1995; Ghosh et al, 2011). Consistently, we also detect changes in upstream regulators of the Raf-MEK-ERK cascade such as the tropomyosin-receptor-kinase (Trk) receptor, the accessory protein son of sevenless (SOS) and the signaling protein SNT, known to be associated with Trk receptors, GRB2-associated-binding protein 1 (GAB1), and Phospholipase C Gamma 1 (PLC γ 1). Further studies will be required to elucidate the role of the Raf-MEK-ERK pathway in NGF-withdrawal induced neuronal death.

Membrane localization controls MAPK activity

Although kinases are mainly localized in the cytosol, a recent mapping of the subcellular localizations of the kinome have shown that kinases are abundantly present in intracellular membrane compartments (Zhang et al, 2021). Kinase localization has been shown to be critical in mediating kinase activity. For example, ectopic recruitment of MAPKs such as Raf to the plasma membrane has been shown to be sufficient to trigger kinase activation in cell lines (Leevers et al, 1994; Stokoe et al, 1994). An important membrane recruitment mechanism is protein palmitoylation, a lipid modification that not only promotes protein membrane association, but also controls protein stabilization and facilitates protein–protein interaction to form local signaling platforms in numerous cell types including neurons (Charollais & Van Der Goot, 2009; Salaun et al, 2010). Compared with other lipid modifications, palmitoylation is reversible and allows proteins to shuttle between cellular compartments, allowing protein relocation within cellular compartments (Iwanaga et al, 2009). In this study, we found that DLK responds to NGF deprivation by increasing its palmitoylation and vesicle recruitment. Interestingly, stress has been shown to increase the levels of palmitoylation of synaptic proteins and influence the palmitoylation of several neuronal kinases, including the calcium/calmodulin-dependent protein

kinase II (CaMKII), protein kinase C (PKC), and Src (Zamzow et al, 2019; Zareba-Kozioł et al, 2019). Therefore, it is interesting to speculate that a global increase in protein palmitoylation may help the recruitment and activation of signaling proteins such as DLK in response to stress.

Endocytosis and sphingomyelin drive DLK activation

DLK functions as a damage sensor in the axon and can initiate the JNK-dependent stress response (Hirai et al, 2005; Chen et al, 2008; Miller et al, 2009; Ghosh et al, 2011; Shin et al, 2012; Watkins et al, 2013). In this study, we show that DLK localizes to axonal vesicles within the secretory and endocytic pathway. Using unbiased lipidomic approach, we found that DLK is enriched in sphingomyelin-containing vesicles. The subcellular distribution of DLK in cultured cells is consistent with the Golgi and vesicular localization described previously for sphingomyelin (Deng et al, 2016). Our results demonstrate that sphingomyelin levels control DLK localization and activation in response to NGF deprivation in DRG neurons. Interestingly, sphingomyelins, together with cholesterol, can form lipid microdomain on the plasma membrane to recruit palmitoylated proteins (Lingwood & Simons, 2010; Delint-Ramirez et al, 2011; Kim et al, 2013; Levental & Veatch, 2016; Tripathi et al, 2021). In addition, the levels of sphingomyelin in these lipid rafts regulate the localization and trafficking of palmitoylated proteins (Xiong et al, 2019). It is therefore tempting to speculate that neuronal stress may cause accumulation of sphingomyelin in intracellular vesicles that favors the recruitment of palmitoylated DLK, promoting kinase activation and neuronal degeneration.

We also found that the formation of new vesicles from the plasma membrane through endocytosis plays an important role in controlling DLK activation. Inhibition of endocytosis blocks DLK vesicle localization and downstream signaling pathway, protecting neurons from different stressors such as NGF withdrawal and

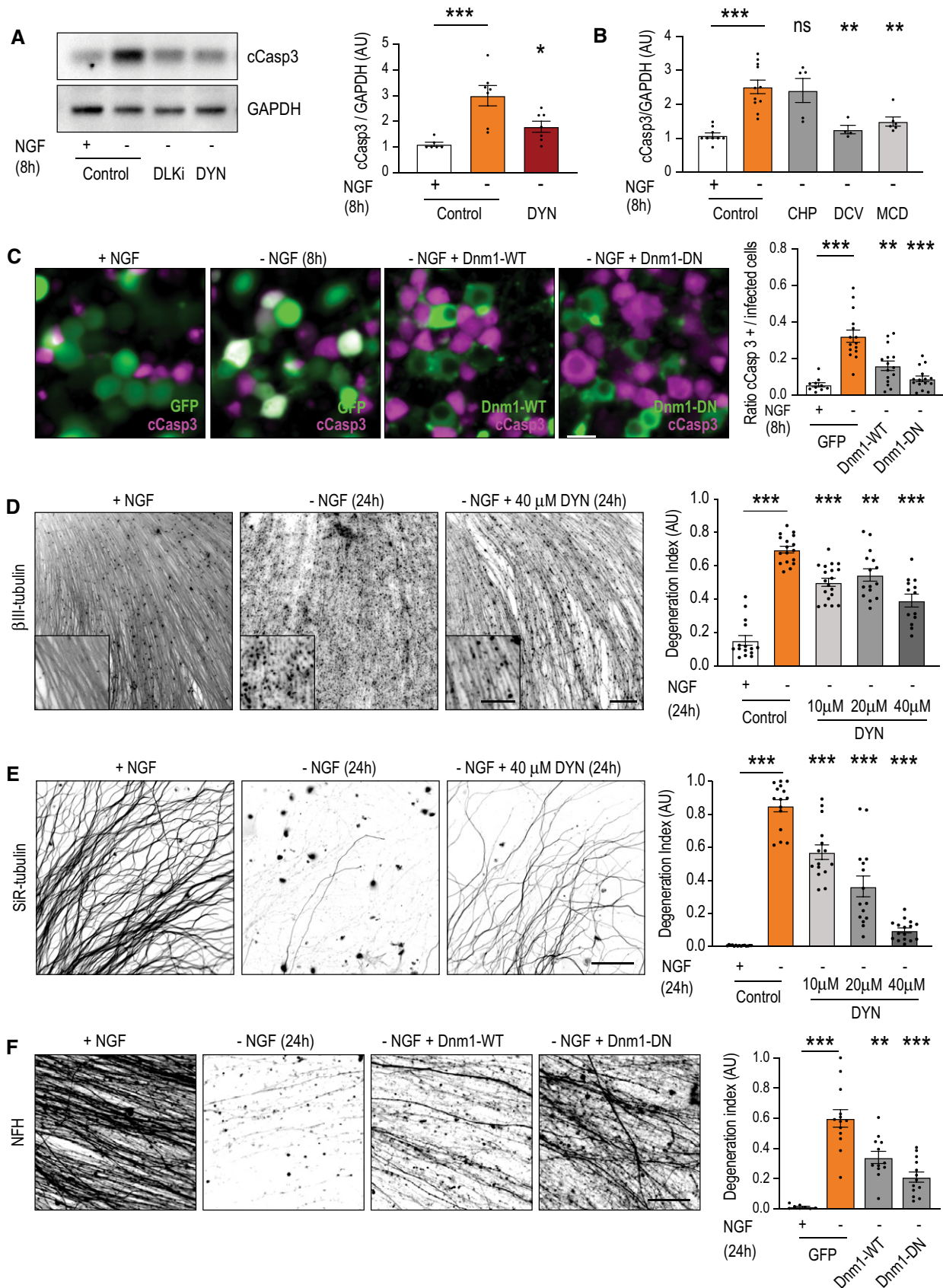


Figure 6.

Figure 6. Inhibition of endocytosis protects against neuronal apoptosis and axon degeneration.

- A Western blot analysis of cleaved caspase-3 (cCasp3) and GAPDH, and quantifications of cCasp3 levels in 3DIV cultured embryonic DRG neurons treated with dynasore (DYN) for 8 h in the absence of NGF ($n = 6\text{--}13$ biological replicates, series of unpaired *t*-test/Mann–Whitney *U* tests with control NGF withdrawal followed by a Holm–Sidak correction).
- B Quantifications of cCasp3 levels from 3DIV DRG neurons treated with chlorpromazine (CHP), dansylcadaverine (DCV) or methyl- β -cyclodextrin (MCD) for 8 h in absence of NGF ($n = 6\text{--}13$ biological replicates, series of unpaired *t*-test/Mann–Whitney *U* tests with control NGF withdrawal followed by a Holm–Sidak correction).
- C Representative images of DRG neurons expressing GFP, Dnm-1-WT-HA or Dnm1-DN-HA form, cultured in the absence of NGF for 8 h, and stained with antibodies against cCasp3 (magenta) and HA tag (green). On the right, quantification of the ratio of cCasp3 positive cells over GFP or HA positive cells ($n = 10\text{--}15$ images from 3 independent cultures, series of unpaired *t*-test/Mann–Whitney *U* tests with control NGF withdrawal followed by a Holm–Sidak correction).
- D Representative images of axons from E12.5 DRG explants cultured for 2 days, subsequently deprived of NGF and treated with different concentrations of dynasore (DYN) for 24 h, and visualized by immunostaining for β III-tubulin. Quantification of the axonal degeneration index as the ratio of fragmented axon area over total axon area ($n = 13\text{--}15$ explants, series of unpaired *t*-test/Mann–Whitney *U* tests with control NGF withdrawal followed by a Holm–Sidak correction).
- E Representative images of axons from cultured embryonic DRG neurons cultured for 2 days, subsequently deprived of NGF and treated with different concentrations of dynasore (DYN) for 24 h, and visualized by imaging SiR-tubulin probe. On the right, quantification of fragmented axons using the degeneration index ($n = 15$ images from three independent cultures, series of unpaired *t*-test/Mann–Whitney *U* tests with control NGF withdrawal followed by a Holm–Sidak correction).
- F Representative images of axons from cultured embryonic DRG neurons expressing GFP, Dnm-1-WT-HA or Dnm1-DN-HA form and deprived of NGF for 24 h, and visualized with an antibody against neurofilament heavy chain (NFH). On the right, quantification of fragmented axons using the degeneration index in ($n = 8\text{--}13$ images from three independent cultures, series of unpaired *t*-test with control NGF withdrawal followed by a Holm–Sidak correction).

Data information: All graphs represent mean \pm SEM. * $P < 0.05$ ** $P < 0.01$ and *** $P < 0.001$. Scale bar represents 100 μ m in (E), 40 μ m in (F), 20 μ m in (C) and (D) and 10 μ m in zooms in (D). See also Figure Appendix Fig S4.

Source data are available online for this figure.

vincristine-mediated microtubule depolymerization. The process of endocytosis may provide the required membrane patches necessary for DLK recruitment and activation. However, we cannot rule out that an extracellular stimulus or a receptor signal during membrane internalization may also be involved in DLK activation. Consistent with the role of endocytosis in controlling DLK signaling pathway, protective effects of endocytosis inhibition have been described to be neuroprotective after spinal cord injury in rats (Li *et al*, 2017). All these data together suggest that protein palmitoylation and membrane internalization are two independent but interrelated pathways involved in the control of the DLK-mediated stress response. Our data show that, upon stress, neurons increase DLK palmitoylation that facilitates the recruitment of the kinase to axonal vesicles. While DLK vesicle recruitment might be exclusively controlled by the increase in DLK palmitoylation, the number of sphingomyelin-positive vesicles available for DLK association may increase the strength or duration of the stress response.

Stress-induced DLK-vesicle assemblies

We found that recruitment of DLK to ectopic intracellular membranes is sufficient to mediate kinase activation, suggesting that local accumulation of DLK is a critical step in stress response signaling. Interestingly, protein assemblies such as liquid–liquid phase separation condensates and cytoplasmic protein granules have been previously identified as critical signaling hubs (Wu, 2013; Zhang *et al*, 2020; Tulpule *et al*, 2021). Our data suggest that stress-induced DLK-vesicle assemblies in the axon signal to the cell body to activate transcriptional responses.

How does DLK in the axon communicate with the neuronal soma? DLK and JNK3 have been suggested to be retrogradely transported in the same vesicle from damaged axons to neuronal cell bodies (Holland *et al*, 2016; Niu *et al*, 2022). Here, we show that DLK localizes to vesicles that are transported bidirectionally along the axon in DRG neurons but do not observe an increase in retrograde DLK-positive vesicles trafficking upon stress. However, we do not rule out a role for DLK in retrograde axonal stress signaling. In our live cell imaging experiments, we are unable to discriminate

between vesicles containing active or inactive DLK. It is therefore possible that only active DLK is retrogradely transported, whereas a constant anterograde transport of inactive DLK is maintained in neurons. Consistent with this idea is that expression of inactive forms of DLK such as a kinase-dead point mutant or a leucine zipper domain mutant localize to vesicles. Alternatively, DLK might not be retrogradely transported itself and other downstream effector such as MKK4 or JNK3 could travel back to the soma to initiate the transcriptional response (Perlson *et al*, 2010). It will be interesting to analyze the localization, activation, and transport of the different components of the DLK signaling cascade to identify how the signal is retrogradely transported to the nucleus to initiate a transcriptional response to stress.

DLK inhibition has been proposed as a neuroprotective strategy as pharmacological inhibition and genetic knockout of DLK confer striking neuroprotection in different chronic forms of stress that include mechanical axon transection or stress associated with drugs that alter the microtubule cytoskeleton such as vincristine or colchicine. DLK also plays a role in animal models of Parkinson's disease, Alzheimer, amyotrophic lateral sclerosis, diffuse traumatic brain injury, excitotoxicity-induced degeneration, glaucoma/optic neuropathy, chemotherapy-induced peripheral neuropathy, or sciatic nerve injury (Chen *et al*, 2008; Miller *et al*, 2009; Pozniak *et al*, 2013; Watkins *et al*, 2013; Fernandes *et al*, 2014; Patel *et al*, 2015; Le Pichon *et al*, 2017; Welsbie *et al*, 2013; Welsbie *et al*, 2017; Welsbie *et al*, 2019; Wlaschin *et al*, 2018; Hu *et al*, 2019; Ma *et al*, 2021). An alternative strategy to inhibit DLK could be to target regulatory features that control DLK localization, such as palmitoylation. These ideas are in line with published work that identifies novel inhibitors of DLK palmitoylation such as ketoconazole. This compound affects DLK localization and blocks phosphorylation of c-Jun upon NGF deprivation (Martin *et al*, 2019). These results further emphasize the idea that DLK-vesicle recruitment is a critical event in stress-induced signaling in DRG neurons.

In summary, our findings show the importance of MAPK localization in controlling kinase activation and highlights DLK as a unique MAPK that is a critical mediator of neurodegeneration.

This study also provides new insights into the mechanism of DLK activation. We propose a model in which inactive DLK is present in the cytosol and at low levels attached to axonal transport vesicles. Upon stress, DLK increases its palmitoylation levels, accumulates at sphingomyelin-positive vesicles, and forms signaling platforms to promote apoptosis and axon degeneration. Endocytosis may increase the number of vesicles available for DLK accumulation which may control the strength and duration of the stress response. These data establish DLK-vesicular assemblies as dynamically regulated platforms for signaling during neuronal stress responses.

Methods and Protocols

Experimental models

Animals

Timed pregnant CD1 mice were obtained from Charles River. The animals were kept under conditions of 50% humidity and a 12 h:12 h light: dark cycle. They were fed a standard pellet diet and tap water ad libitum. All animal studies were authorized and approved by the Genentech Institutional Animal Care and Use Committee.

Primary neuronal cultures and NGF withdrawal

E12.5 - E13.5 CD-1 mouse embryos were dissected in Leibovitz's L-15 to isolate the DRGs. Neurons were dissociated with 0.05% trypsin (Sigma) for 30 min at 37°C and plated on precoated poly-D-lysine (PDL) and laminin chamber slides (BioCoat; BD), or chambered coverslip (Ibidi) and plates coated with 0.1 mg/ml PDL (Sigma) and 1 µg/ml laminin (Invitrogen). DRG neurons were plated at a density of 125,000 cells per well (8 well slides or 48 well plates) for biochemistry experiments or in small dots with 30,000 cells/ dot for immunofluorescence and live imaging experiments. Explants were obtained from E12.5 to E13.5 CD-1 mouse embryos and directly plated on PDL/laminin-coated plates. Explants and dissociated DRG neurons were cultured in F12 media containing N3 supplement, 40 mM glucose, and 50 ng/ml NGF, at 37°C in 5% CO₂. Twenty-four hour after plating, media was supplied with 7 mM mitotic inhibitor (cytosine arabinofuranoside) and kept it for 48 h.

Dissociated DRG neurons in suspension were nucleofected with 500 ng of siRNAs using the Amaxa Mouse Neuron Nucleofector kit (Lonza) according to the manufacturer's instructions. Adherent DRG neurons were transduced with AAV (Dj serotype) at 3 DIV for 3–7 days.

DRGs were cultured for 3 days (for Western blot and immunofluorescence experiments) or 7 days (live imaging and Dnm-1 overexpressing experiments) before treatments. For NGF withdrawal, media was replaced with media containing no NGF and 25 µg/ml anti-NGF antibody (Genentech) for various time periods (3, 8 or 24 h).

Heterologous cell culture and transfection

HeLa cells were obtained from ATCC and all stocks were tested for mycoplasma prior to and after cells were cryopreserved. Two methods were used to avoid false-positive/-negative results: Mycosensor PCR Assay kit (302108, Agilent) and MycoAlert Mycoplasma

Detection Kit (LT07-318, Lonza). They were not authenticated prior to use.

Cells were cultured in DMEM: F12 supplemented with 10% fetal bovine serum (VWR), 2 mM L-glutamine, penicillin (100 units/ml) and streptomycin (100 µg ml⁻¹) (Invitrogen) at 37°C and 5% CO₂. Cells were plated in 24-well plates with or without 18 mm glass coverslips, and transfected using 0.25 µg of DNA and 0.75 µl of Fugene HD (Promega) according to the manufacturer's protocol. For immunofluorescence experiments, cells with low expression levels of the different constructs were used.

Method details

Quantification of proteome and phosphoproteome by mass spectrometry

Protein precipitation

Protein concentration in the lysates was quantified using the Pierce micro-BCA assay (ThermoFisher Scientific, Waltham, MA). Cysteines were reduced with 5 mM dithiothreitol and alkylated with 15 mM Iodoacetamide (Sigma). All protein from the cell lysates was precipitated with a combination of methanol/chloroform/water (Wessel & Flügge, 1984). In brief, X volume of lysate was mixed with 4× volume of methanol followed by 2× volume of chloroform and 3× volume of water. The protein pellets were washed a total of three times with 5× volume of methanol. The protein pellets were air dried and resuspended in 6 M guanidine-HCl, 100 mM EPPS pH 8.0.

LysC/trypsin digestion

The protein in 6 M guanidine-HCl/EPPS was diluted to 2 M guanidine-HCl with 100 mM EPPS, pH 8.0. 1 mg of protein/sample was digested at 25°C for 12 h with lysyl endopeptidase (LysC, Wako Chemicals USA) at a 1:25; protein:protease ratio. Following LysC digestion, the peptides in 4 M urea were diluted to 0.5 M guanidine-HCl with 100 mM EPPS, pH 8.0. The lysC peptides were digested with trypsin at 37°C for 8 h (Promega) at a 1:50; protein:protease ratio.

TMT labelling of peptides

0.5 mg of peptide from each sample was labeled with 1.2 mg of TMT reagent resuspended in 30 µl, 100% acetonitrile. The peptides were incubated with TMT reagent for 3 h at 25°C. TMT-labeled peptides were quenched with hydroxylamine (0.5% final) and acidified with trifluoroacetic acid (2% final). The samples were combined, desalted with 200 mg tC18 Sep-Paks, and dried by vacuum.

Phosphoserine, -threonine, -tyrosine enrichment and fractionation

Phosphotyrosine (pY) peptides were enriched using the Cell Signaling Technologies P-Tyr-1000 antibody kit as per the manufacturers' protocol. The flow through from the pY enrichment was desalted on a 200 mg tC18 Sep-Pak cartridges (Waters Corporation, Milford, MA) and dried by centrifugal evaporation and saved for phosphoserine and phosphothreonine (pST) analysis. pST phosphopeptides were enriched using the Pierce Fe-NTA phospho-enrichment kit (ThermoFisher). In brief, peptides were bound and washed as per the manufacturers' protocol. Phosphopeptides were eluted from the Fe-NTA resin with 50 mM HK2PO4 pH 10.5. Labeled

Phosphopeptides were subjected to orthogonal basic-pH reverse phase fractionation on a 3×100 mm column packed with $1.9 \mu\text{m}$ Poroshell C18 material (Agilent, Santa Clara, CA), equilibrated with buffer A (5% acetonitrile in 10 mM ammonium bicarbonate, pH 8). Peptides were fractionated utilizing a 45 min linear gradient from 8% to 30% buffer B (90% acetonitrile in 10 mM ammonium bicarbonate, pH 8) at a flow rate of 0.4 mL/min. Ninety-six fractions were consolidated into 24 samples, acidified with formic acid and vacuum dried. The samples were resuspended in 0.1% trifluoroacetic acid, desalted on StageTips and vacuum dried. Peptides were reconstituted in 5% formic acid + 5% acetonitrile for LC-MS3 analysis. The flow through peptides from the pST enrichment were saved for total protein analysis.

Peptide fractionation for total protein analysis

The flow through from the pST enrichment was dried by centrifugal evaporation. The dried peptides were resuspended in 0.1% TFA. Approximately 250 μg of peptide mix was subjected to orthogonal basic-pH reverse phase fractionation on a 3×100 mm column packed with $1.9 \mu\text{m}$ Poroshell C18 material (Agilent, Santa Clara, CA), equilibrated with buffer A (5% acetonitrile in 10 mM ammonium bicarbonate, pH 8). Peptides were fractionated utilizing a 45 min linear gradient from 12 to 45% buffer B (90% acetonitrile in 10 mM ammonium bicarbonate, pH 8) at a flow rate of 0.4 ml/min. Ninety-six fractions were consolidated into 24 samples, acidified with formic acid and vacuum dried. The samples were resuspended in 5% formic acid, desalted on StageTips, and vacuum dried. Peptides were reconstituted in 5% formic acid + 5% acetonitrile for LC-MS3 analysis.

Mass spectrometry analysis

All peptide mass spectra were acquired on an Orbitrap Fusion Lumos coupled to an EASY nanoLC-1000 (or nanoLC-1200) (ThermoFisher) liquid chromatography system. Approximately 2 μg of peptides were loaded on a $75 \mu\text{m}$ capillary column packed in-house with Sepax GP-C18 resin ($1.8 \mu\text{m}$, 150 \AA , Sepax) to a final length of 35 cm. Peptides for total protein analysis were separated using a 90-min linear gradient from 10 to 28% acetonitrile in 0.1% formic acid. The mass spectrometer was operated in a data-dependent mode. The scan sequence began with FTMS1 spectra (resolution = 120,000; mass range of 350–1,400 m/z ; max injection time of 50 ms; AGC target of $1e6$; dynamic exclusion for 60 s with a ± 10 ppm window). The ten most intense precursor ions were selected for ITMS2 analysis via collisional-induced dissociation (CID) in the ion trap (normalized collision energy (NCE) = 35; max injection time = 100 ms; isolation window of 0.7 Da; AGC target of $2e4$). Following ITMS2 acquisition, a synchronous-precursor-selection (SPS) MS3 method was enabled to select 10 MS2 product ions for high energy collisional-induced dissociation (HCD) with analysis in the Orbitrap (NCE = 55; resolution = 50,000; max injection time = 110 ms; AGC target of $1.5e5$; isolation window at 1.2 Da for +2 m/z , 1.0 Da for +3 m/z or 0.8 Da for +4 to +6 m/z).

pY peptides were separated using a 180-min linear gradient from 7 to 26% acetonitrile in 0.1% formic acid. The mass spectrometer was operated in a data-dependent mode. The scan sequence began with FTMS1 spectra (resolution = 120,000; mass range of 350–1,400 m/z ; max injection time of 50 ms; AGC target of $1e6$; dynamic

exclusion for 75 s with a ± 10 ppm window). The ten most intense precursor ions were selected for FTMS2 analysis via collisional-induced dissociation (CID) in the ion trap (normalized collision energy (NCE) = 35; max injection time = 150 ms; isolation window of 0.7 Da; AGC target of $3e4$; m/z = 2–6; Orbitrap resolution = 15k). Following FTMS2 acquisition, a synchronous-precursor-selection (SPS) MS3 method was enabled to select five MS2 product ions for high energy collisional-induced dissociation (HCD) with analysis in the Orbitrap (NCE = 55; resolution = 50,000; max injection time = 300 ms; AGC target of $1e5$; isolation window at 1.2 Da).

pST peptides were separated using a 120-min linear gradient from 6 to 26% acetonitrile in 0.1% formic acid. The mass spectrometer was operated in a data-dependent mode. The scan sequence began with FTMS1 spectra (resolution = 120,000; mass range of 350–1,400 m/z ; max injection time of 50 ms; AGC target of $1e6$; dynamic exclusion for 60 s with a ± 10 ppm window). The ten most intense precursor ions were selected for ITMS2 analysis via collisional-induced dissociation (CID) in the ion trap (normalized collision energy (NCE) = 35; max injection time = 200 ms; isolation window of 0.7 Da; AGC target of $2e4$). Following MS2 acquisition, a synchronous-precursor-selection (SPS) MS3 method was enabled to select five MS2 product ions for high energy collisional-induced dissociation (HCD) with analysis in the Orbitrap (NCE = 55; resolution = 50,000; max injection time = 300 ms; AGC target of $1e5$; isolation window at 1.2 Da for +2 m/z , 1.0 Da for +3 m/z or 0.8 Da for +4 to +6 m/z).

All mass spectra were converted to mzXML using a modified version of ReAdW.exe. MS/MS spectra were searched against a concatenated 2018 mouse Uniprot protein database containing common contaminants (forward + reverse sequences) using the SEQUEST algorithm (Eng et al, 1994). Database search criteria are as follows: fully tryptic with two missed cleavages; a precursor mass tolerance of 50 ppm and a fragment ion tolerance of 1 Da for peptide and phosphoserine and phosphothreonine (phosphotyrosine fragment ion tolerances were set to 0.02 Da); oxidation of methionine (15.9949 Da) or pSTY (79.9663304; pSTY searches only) was set as differential modifications. Static modifications were alkylation on cysteines (57.02146374) and TMT on lysines and N-termini of peptides (229.1629). Peptide-spectrum matches were filtered using linear discriminant analysis (Huttlin et al, 2010) and adjusted to a 1% peptide false discovery rate (FDR) (Elias & Gygi, 2007) and collapsed further to a final 1.0% protein-level FDR. Posttranslational modifications were localized using a probability-based algorithm similar to Ascore (Beausoleil et al, 2006). Proteins were quantified by summing the total reporter intensities across all matching PSMS.

Immunoprecipitation of DLK-containing vesicles for lipidomic analysis

HeLa cells were plated in 15 cm dishes and transfected with 15 $\mu\text{g}/\text{plate}$ of DNA for 24 h. Cell were quickly rinsed twice with PBS, scraped in 1 ml of PBS containing protease and phosphatase inhibitors and gently homogenized with 20 strokes of a 2 ml homogenizer. The homogenate was centrifuged at 1,000 rpm for 2 min at 4°C. Supernants were precleared with magnetic beads for 10 min at RT and anti-HA Magnetic Beads were blocked with 3% BSA/PBS for 30 min at RT. Precleared supernants and blocked beads were

incubated for 10 min at RT in constant rotation. Beads were washed 5 times with PBS and subjected to lipidomic analysis.

Lipid extraction of DLK-containing beads

For lipid extraction, 800 μ l of dichloromethane/methanol (1:1, v/v) was added into each vial containing magnetic beads. The vials were then sonicated for 2 min in ultrasonic bath sonicator. Then, 100 μ l of pre-mixed internal standard (SCIEX, cat#: 5040156) were spiked into each extract, mixed by vortex, and centrifuged for 10 min. Using a magnetic tray to pull down the beads, the supernatant was transferred to a new glass vial. The extracts were then dried by vacuum evaporation and reconstituted with 250 μ l of dichloromethane/methanol (1:1 v/v, 10 mM ammonium acetate). Lipid analysis was performed on a SelexION enabled 6500 QTRAP (Sciex, Redwood City, CA) utilizing Lypidizer platform methods (Sciex).

DNA and shRNA constructs

DNA constructs were designed by the authors, and constructed and packaged into AAV-DJ viruses by Vectorbuilder. The endoplasmic reticulum membrane targeting sequence of VAPB was taken from (Teuling *et al*, 2007) and the membrane targeting sequence (MTS) of the ActA protein of *Listeria monocytogenes* was taken from (Pistor *et al*, 1994). The C-terminal CAAX motif was taken from human K-Ras4B (aa 169–188).

Live imaging experiments

Live-cell imaging experiments were performed on a 3i Marianas spinning disk confocal microscope equipped with a Yokogawa CSU-W1 spinning disc, a Photometrics Prime95B CMOS camera, Zeiss Definite Focus 2, OkoLab stage-top environmental control chamber, a 150 mW 488 nm solid state laser passed through a 3i Mesa W excitation enhancement and a Zeiss 63 \times Plan Apo 1.4 NA objective. The system was controlled by the 3i Slidebook 6 software. Chambered coverslips (Ibidi) were imaged using an incubation chamber that maintains temperature and CO₂ at 37°C and 5% CO₂. Neuron live imaging was performed in full conditioned medium and fresh medium was added to HeLa before imaging.

Time-lapse live-cell imaging of GFP-tagged N-terminal domain of DLK and DLK wild-type, kinase dead mutant, leucine zipper domain mutant and a palmitoyl-site mutant was performed with minimal 488 nm excitation with time acquisition intervals of 500 ms for 1–2 min.

Axon integrity in dissociated neurons was assessed by incubating neurons with SiR-tubulin (100 nM in full conditioned medium) for 5 min at 37°C before imaging. Mitochondrial integrity after dynasore treatments was assessed by incubating neurons with MitoTracker Green FM (25 nM in full conditioned medium) for 5 min at 37°C before imaging. In each case, five single images were taken from each dot of dissociated neurons at similar distance from soma center.

Live cell imaging of D609 and dynasore treatments was performed in 3DIV cultured embryonic neurons by incubating neurons with the Live Cell Labeling dye for 1 h in a 37°C, 5% CO₂ incubator. Media was replaced and neurons were imaged. In each case, five single images were taken from each dot of dissociated neurons.

Subcellular fractionation

Membrane and cytosolic subcellular fractions were obtained from 3DIV cultured embryonic DRG neurons or HeLa cells ($\sim 0.5 \times 10^6$ cells per condition) using the Mem-PER Plus Membrane Protein Extraction Kit (Thermo Fisher) according to the manufacturer's instructions. Briefly, cells were washed with Cell Wash Solution and resuspended in 150 μ l of Permeabilization Buffer. Samples were briefly vortexed and incubated 10 min at 4°C with constant mixing. After 15 min of centrifugation at 16,000 g, supernatants were transferred to a new tube (cytosolic fraction) and pellet was resuspended in 150 μ l of Solubilization Buffer. The samples were incubated at 4°C for 30 min with constant mixing and centrifuged at 16,000 g for 15 min at 4°C. Resultant supernatants were considered the membrane and membrane-associated proteins. Pellets were considered as insoluble fractions. Fraction purity was assessed by Western blot analysis using antibodies against α -tubulin and STMN-1 for the cytosolic fraction and Na⁺/K⁺-ATPase and STMN-2 as membrane markers.

Click-it assay

Click-it assays were performed in 3DIV cultured embryonic DRG neurons (10⁶ neurons per condition). 100 μ M of Click-iT palmitic acid-azide was added to the cell medium and incubated at 37°C and 5% CO₂. After 4-h incubation, the medium was removed and cells were lysated in 200 μ l of lysis buffer (1% sodium dodecyl sulfate in 50 mM Tris-HCl, pH 8.0) containing protease and phosphatase inhibitors. Cells were incubated for 20 min on ice, vortexed for 5 min and cell lysate was centrifuged at 18,000 g, 4°C for 5 min. 50 μ l of supernatant was subjected to a click-chemistry reaction in the presence of a biotin-alkyne using the Click-iT Protein Reaction Buffer Kit (Thermo Fisher) and following the manufacturer's instructions. Biotinylated proteins were pulled down using streptavidin magnetic beads (25 μ l/reaction) in a lysis buffer containing 20 mM Tris-HCl, pH 7.5, 150 mM NaCl, 1% Triton X-100, and protease inhibitors overnight at 4°C. After 4 washes with lysis buffer, pellets were resuspended in LDS sample buffer containing sample reducing agent, boiled for 10 min and subjected to immunoblotting detection for DLK.

Immunoblotting

Neurons and cell lines were directly lysed in LDS sample buffer containing sample reducing agent, boiled for 10 min and run in NuPAGE Bis-Tris gradient gels (Thermo Fisher) followed by blotting on nitrocellulose membranes using a dry blotting setup (iBlot 2 Gel Transfer Device, Thermo Fisher). After 1 h blocking in 5% BSA/TBST buffer, membranes were incubated with primary antibodies overnight at 4°C and secondary HRP-conjugated antibodies for 1 h at room temperature. Chemiluminescence signals were acquired on ChemiDoc XRS+ (Bio-Rad) and quantified using Image J software.

Immunofluorescence staining and imaging

Cells were fixed with 4% PFA/4% sucrose/PBS, washed three times for 5 min in PBS, permeabilized with PBS/0.1% Triton X-100 for 15 min and blocked with 10% FBS/PBS blocking solution for 1 h.

Subsequently, cells were incubated with primary antibodies overnight at 4°C. After three washes with PBS, cells were incubated with secondary-antibodies in blocking buffer for 1 h at room temperature. After washing, coverslips were mounted in Fluoromount-G (Electron Microscopy Sciences).

Images of HeLa cells and dissociated DRG neurons were captured with a Zeiss LSM 710 inverted confocal laser-scanning microscope (Zeiss) with a 100X Plan-Apochromat NA 1.46 oil DIC, Plan-Apochromat 40X NA1.40 Oil DIC and a Plan-Apochromat 20X NA 0.8 objective. Each confocal image was a z series of 5–10 images with a 0.3 µm steps and averaged two times, covering the entire region of interest from top to bottom. Maximum projections were done from the resulting z stack. Images for colocalization analysis were deconvolved with Huygens software (Scientific Volume Imaging, The Netherlands, <http://svi.nl>). DRG explants were imaged on a Keyence BZ-X 700 fluorescence microscope equipped with a 20X Nikon CFI Plan Apo NA 0.75 objective. Images were taken from each dot at similar distance from soma center.

For fluorescence intensity comparison, settings were kept the same for all conditions. All images were processed and analyzed with ImageJ.

Drug treatments

The following concentrations were used for 4-h treatments: brefeldin A: 5 µg/ml, 2-bromopalmitate: 30 µM, dynasore: 80 µM, chlorpromazine: 25 µg/ml, dansylcadaverine: 300 µM; β-methylcyclodextrin: 5 mM, D609: 50 µM, DLKi: 1 µM, vincristine: 100 nM.

The following concentrations were used for 8-h treatments: dynasore: 80 µM, chlorpromazine: 7 µg/ml, dansylcadaverine: 30 µM, β-methylcyclodextrin: 5 mM. For 24 h treatments, dynasore was used at 10, 20, and 40 µM.

LDH assay

Cytotoxicity was determined by measuring the levels of lactate dehydrogenase (LDH) released in the media using the CyQUANT™ LDH Cytotoxicity Assay, according to the manufacturer's instructions. DRG neurons were plated in 96-well plates at a density of 6×10^4 neurons per condition, cultured for 3 days and treated with control or D609 for 3 h. To measure the maximum LDH release, lysis buffer was added to the well 30 min before collecting the media. Quantifications were performed in duplicates from three independent cultures.

Image analysis and quantification

Data were collected and analyzed from 3 to 5 independent experiments. No specific strategy for randomization and/or stratification was employed. The studies were blind in data processing and analysis. Grubbs' test was performed to detect significant outliers.

Analysis of knockdowns

DRG neurons were nucleofected with either non-targeting siRNA control or a siRNA against DLK. Neurons were fixed 72 h after nucleofection with 4% PFA/4% sucrose/PBS and co-stained with an antibody against DLK together with an anti-β-III tubulin antibody.

Mean intensities for DLK were quantified using ImageJ software. Background values were subtracted and values were corrected to β-III tubulin levels.

Object-based colocalization analysis

Work on centers-particles coincidence analysis was determined using the JACoP plugin under ImageJ software from deconvolved images of each channel. For each condition, five images from three independent experiments were analyzed. Analyses were repeated rotating DLK images 90 degrees as control.

Pearson's coefficient quantification

Pearson's coefficient and Costes randomization analysis were determined using the JACoP plugin under ImageJ software from deconvolved images of each channel. For each condition, five images from three independent experiments were analyzed.

Quantification of moving particles

DLK-positive vesicles (labeled with GFP-tagged N-terminal domain of DLK, DLK wild-type, kinase dead mutant, leucine zipper domain mutant and a palmitoyl-site mutant version of DLK) were quantified from kymographs of axons created using the KymoResliceWide v.0.5 plugin under Fiji.

Quantification of DLK-positive vesicles in fixed images

ImageJ plugin ComDet was used to quantify the number of DLK-positive vesicles in axons. Numbers were normalized to the corresponding neurite length.

Quantification of Western blot data

Densitometry of Western blots was performed using the gel analysis module of ImageJ software. Protein levels were normalized to loading controls. Ratio of membrane and cytosolic protein was calculated as the ratio of protein present in the membrane or cytosolic fraction to the protein content of both fractions.

Axon degeneration index

The axon degeneration index from tubulin, SiR-tubulin and neurofilament heavy chain stained images of axons was calculated based on a method described previously (Sasaki *et al*, 2009). Following background subtraction, each image was binarized based on pixel intensity to create a map of axon area. To detect degenerated axons, we used the particle analyzer module of ImageJ and counted the area of the small fragments or particles (size = 20–10,000 pixels) derived from the degenerated axons. Axon degeneration index was calculated as a ratio of fragmented axons area over the total axon area in each image.

Caspase-3 staining

Following background subtraction, cCasp-3, HA and GFP images were binarized based on pixel intensity to create a map of

infected (HA- or GFP-positive cells) and cCasp-3 positive cells. Cells containing both infected and cCasp-3 signal were calculated using the image calculator, watershed segmentation and particle analyzer module of Image J. The ratio of infected neurons positive for cCasp-3 over the total amount of cells infected was calculated.

Statistical analysis

All statistical details of experiments, including the definitions and exact values of *n*, and statistical tests performed, can be found in Figures and Figure Legends. Data processing and statistical analysis were made in Excel and GraphPad Prism (GraphPad Software). Significance was defined as: ns-not significant, **P* < 0.05 ***P* < 0.01 and ****P* < 0.001. Statistical analyses include: Unpaired *t*-test, Mann–Whitney *U* test, one-way ANOVA followed by a Tukey's multiple comparison test, Kruskal–Wallis test followed by a Dunn's Multiple Comparison Test and Holm–Sidak correction. Groups with all zero or negative values were excluded from the analysis. The assumption of normality was checked using Shapiro–Wilk test.

Statistical testing of proteomics data

Quantification and statistical testing of global proteomics and phosphoproteomics data were performed by MSstats v2, an open-source R/Bioconductor package (Choi *et al*, 2014). MSstats was used to create statistical testing results on the protein and site level for the global proteomics and phosphoproteomics datasets, respectively, using the Peptide Spectrum Matches (PSM) as described above. First, PSMs were filtered out if they were from decoy proteins; from peptides with length < 7; with isolation specificity < 70%; with reporter ion intensity less than 2^{eight} noise estimate; with summed reporter ion intensity (across all eleven channels) lower than 30,000. Next, PSMs were summarized to the peptide level by selecting the single PSM per peptide with the highest summed reporter ion intensity across all channels. Multiple fractions per dataset were also combined before analysis in MSstats. PSMs across fractions were selected using the same criteria as described above. Next, MSstats performed protein/site quantitation and differential abundance analysis between experimental conditions based on a linear mixed-effects model per protein (global proteome data) or site (phosphoproteome data) using standard parameters from the package (Choi *et al*, 2014).

Materials availability

Reagents and resources used in this study are listed in the Reagent and Tool Table and may be requested through Genentech's MTA program.

Data availability

The mass spectrometry data from this publication have been deposited in the MassIVE repository (<https://massive.ucsd.edu/ProteoSAFe/static/massive.jsp>) and assigned the identifier MSV000088168.

Expanded View for this article is available online.

Acknowledgements

We thank Meredith Sagolla for performing image deconvolutions. We thank Lilian Phu for helping with the proteomic samples handling. We thank Don Kirkpatrick and Erik Verschuereen for guidance on the proteomic experiments. We thank the Hoogenraad lab for helpful suggestions during the study. The work in this manuscript was funded by Genentech Inc., a member of the Roche Group.

Author contributions

Elena Tortosa: Conceptualization; Data curation; Software; Formal analysis; Supervision; Validation; Investigation; Visualization; Methodology; Writing—original draft; Project administration; Writing—review & editing. **Arundhati Sengupta Ghosh:** Investigation; Methodology. **Qingling Li:** Resources; Methodology. **Weng Ruh Wong:** Resources; Methodology. **Trent Hinkle:** Resources; Formal analysis; Methodology. **Wendy Sandoval:** Resources; Supervision; Methodology. **Christopher M Rose:** Resources; Supervision; Methodology. **Casper C Hoogenraad:** Conceptualization; Supervision; Writing—original draft; Project administration; Writing—review & editing.

Disclosure and competing interests statement

All authors are employees of Genentech, Inc., a member of the Roche group. The authors declare that they have no additional conflict of interest.

References

- Asghari Adib E, Smithson LJ, Collins CA (2018) An axonal stress response pathway: degenerative and regenerative signaling by DLK. *Curr Opin Neurobiol* 53: 110–119
- Asih PR, Prikas E, Stefanoska K, Tan ARP, Ahel HI, Ittner A (2020) Functions of p38 MAP kinases in the central nervous system. *Front Mol Neurosci* 13: 570586
- Beausoleil SA, Villén J, Gerber SA, Rush J, Gygi SP (2006) A probability-based approach for high-throughput protein phosphorylation analysis and site localization. *Nat Biotechnol* 24: 1285–1292
- Brunet A, Roux D, Lenormand P, Dowd S, Keyse S, Pouyssegur J (1999) Nuclear translocation of p42/p44 mitogen-activated protein kinase is required for growth factor-induced gene expression and cell cycle entry. *EMBO J* 18: 664–674
- Charollais J, Van Der Goot FG (2009) Palmitoylation of membrane proteins (Review). *Mol Membr Biol* 26: 55–66
- Chen CH, Wang WJ, Kuo JC, Tsai HC, Lin JR, Chang ZF, Chen RH (2005) Bidirectional signals transduced by DAPK-ERK interaction promote the apoptotic effect of DAPK. *EMBO J* 24: 294–304
- Chen X, Rzhetskaya M, Kareva T, Bland R, During MJ, Tank AW, Kholodilov N, Burke RE (2008) Antiapoptotic and trophic effects of dominant-negative forms of dual leucine zipper kinase in dopamine neurons of the substantia nigra *in vivo*. *J Neurosci* 28: 672–680
- Choi M, Chang CY, Clough T, Broudy D, Killeen T, MacLean B, Vitek O (2014) MSstats: An R package for statistical analysis of quantitative mass spectrometry-based proteomic experiments. *Bioinformatics* 30: 2524–2526
- Delint-Ramirez I, Willoughby D, Hammond GVR, Ayling LJ, Cooper DMF (2011) Palmitoylation targets AKAP79 protein to lipid rafts and promotes its regulation of calcium-sensitive adenylyl cyclase type 8. *J Biol Chem* 286: 32962–32975
- Deng Y, Rivera-Molina FE, Toomre DK, Burd CG (2016) Sphingomyelin is sorted at the trans Golgi network into a distinct class of secretory vesicle. *Proc Natl Acad Sci USA* 113: 6677–6682

- Deshmukh M, Johnson EM (1997) Programmed cell death in neurons: focus on the pathway of nerve growth factor deprivation-induced death of sympathetic neurons. *Mol Pharmacol* 51: 897–906
- Eblen ST (2018) Extracellular-regulated kinases: signaling from Ras to ERK substrates to control biological outcomes. In *Advances in Cancer Research*
- Elias JE, Gygi SP (2007) Target-decoy search strategy for increased confidence in large-scale protein identifications by mass spectrometry. *Nat Methods* 4: 207–214
- Eng JK, McCormack AL, Yates JR (1994) An approach to correlate tandem mass spectral data of peptides with amino acid sequences in a protein database. *J Am Soc Mass Spectrom* 5: 976–989
- Fernandes KA, Harder JM, John SW, Shrager P, Libby RT (2014) DLK-dependent signaling is important for somal but not axonal degeneration of retinal ganglion cells following axonal injury. *Neurobiol Dis* 69: 108–116
- Formstecher E, Ramos JW, Fauquet M, Calderwood DA, Hsieh J-C, Canton B, Nguyen X-T, Barnier J-V, Camonis J, Ginsberg MH et al (2001) PEA-15 mediates cytoplasmic sequestration of ERK MAP kinase. *Dev Cell* 1: 239–250
- Freeman RS, Burch RL, Crowder RJ, Lomb DJ, Schoell MC, Straub JA, Xie L (2004) NGF deprivation-induced gene expression: after ten years, where do we stand? In *Progress in Brain Research*
- Fukuda M, Gotoh Y, Nishida E (1997) Interaction of MAP kinase with MAP kinase kinase: its possible role in the control of nucleocytoplasmic transport of MAP kinase. *EMBO J* 16: 1901–1908
- Gault CR, Obeid LM, Hannun YA (2010) An overview of sphingolipid metabolism: from synthesis to breakdown. *Adv Exp Med Biol* 688: 1–23
- Ghosh AS, Wang B, Pozniak CD, Chen M, Watts RJ, Lewcock JW (2011) DLK induces developmental neuronal degeneration via selective regulation of proapoptotic JNK activity. *J Cell Biol* 194: 751–764
- Hetman M, Gosdz A (2004) Role of extracellular signal regulated kinases 1 and 2 in neuronal survival. *Eur J Biochem* 271: 2050–2055
- Hirai SI, Katoh M, Terada M, Kyriakis JM, Zon LI, Rana A, Avruch J, Ohno S (1997) MST/MLK2, a member of the mixed lineage kinase family, directly phosphorylates and activates SEK1, an activator of c-Jun N-terminal kinase/stress-activated protein kinase. *J Biol Chem* 272: 15167–15173
- Hirai SI, Kawaguchi A, Suenaga J, Ono M, Cui DF, Ohno S (2005) Expression of MUK/DLK/ZPK, an activator of the JNK pathway, in the nervous systems of the developing mouse embryo. *Gene Expr Patterns* 5: 517–523
- Holland SM, Collura KM, Ketschek A, Noma K, Ferguson TA, Jin Y, Gallo G, Thomas GM (2016) Palmitoylation controls DLK localization, interactions and activity to ensure effective axonal injury signaling. *Proc Natl Acad Sci USA* 113: 763–768
- Hu Z, Deng N, Liu K, Zeng W (2019) DLK mediates the neuronal intrinsic immune response and regulates glial reaction and neuropathic pain. *Exp Neurol* 322: 113056
- Huntwork-Rodriguez S, Wang B, Watkins T, Ghosh AS, Pozniak CD, Bustos D, Newton K, Kirkpatrick DS, Lewcock JW (2013) JNK-mediated phosphorylation of DLK suppresses its ubiquitination to promote neuronal apoptosis. *J Cell Biol* 202: 747–763
- Huttlin EL, Jedrychowski MP, Elias JE, Goswami T, Rad R, Beausoleil SA, Villén J, Haas W, Sowa ME, Gygi SP (2010) A tissue-specific atlas of mouse protein phosphorylation and expression. *Cell* 143: 1174–1189
- Iwanaga T, Tsutsumi R, Noritake J, Fukata Y, Fukata M (2009) Dynamic protein palmitoylation in cellular signaling. *Prog Lipid Res* 48: 117–127
- Kim EK, Choi EJ (2010) Pathological roles of MAPK signaling pathways in human diseases. *Biochim Biophys Acta - Mol Basis Dis* 1802: 396–405
- Kim EK, Choi EJ (2015) Compromised MAPK signaling in human diseases: an update. *Arch Toxicol* 89: 867–882
- Kim KS, Kim JS, Park JY, Suh YH, Jou I, Joe EH, Park SM (2013) DJ-1 associates with lipid rafts by palmitoylation and regulates lipid rafts-dependent endocytosis in astrocytes. *Hum Mol Genet* 22: 4805–4817
- Kristiansen M, Ham J (2014) Programmed cell death during neuronal development: the sympathetic neuron model. *Cell Death Differ* 21: 1025–1035
- Larhammar M, Huntwork-Rodriguez S, Jiang Z, Solanoy H, Sengupta Ghosh A, Wang B, Kaminker JS, Huang K, Eastham-Anderson J, Siu M et al (2017) Dual leucine zipper kinase-dependent PERK activation contributes to neuronal degeneration following insult. *Elife* 6: 1–27
- Le Pichon CE, Meilandt WJ, Dominguez S, Solanoy H, Lin H, Ngu H, Gogineni A, Sengupta Ghosh A, Jiang Z, Lee S-H et al (2017) Loss of dual leucine zipper kinase signaling is protective in animal models of neurodegenerative disease. *Sci Transl Med* 9: aag0394
- Leevers SJ, Paterson HF, Marshall CJ (1994) Requirement for Ras in Raf activation is overcome by targeting Raf to the plasma membrane. *Nature* 369: 411–414
- Levental I, Veatch SL (2016) The continuing mystery of lipid rafts. *J Mol Biol* 428: 4749–4764
- Li G, Shen F, Fan Z, Wang Y, Kong X, Yu D, Zhi X, Lv G, Cao Y (2017) Dynasore improves motor function recovery via inhibition of neuronal apoptosis and astrocytic proliferation after spinal cord injury in Rats. *Mol Neurobiol* 54: 7471–7482
- Lingwood D, Simons K (2010) Lipid rafts as a membrane-organizing principle. *Science* 327: 46–50
- Ma J, Goodwani S, Acton PJ, Buggia-Prevot V, Kesler SR, Jamal I, Mahant ID, Liu Z, Mseeh F, Roth BL et al (2021) Inhibition of dual leucine zipper kinase prevents chemotherapy-induced peripheral neuropathy and cognitive impairments. *Pain* 162: 2599–2612
- Maor-Nof M, Romi E, Shalom HS, Ulisse V, Raanan C, Nof A, Leshkowitz D, Lang R, Yaron A (2016) Axonal degeneration is regulated by a transcriptional program that coordinates expression of pro- and anti-degenerative factors. *Neuron* 92: 991–1006
- Martin DDO, Kanuparthi PS, Holland SM, Sanders SS, Jeong HK, Einarson MB, Jacobson MA, Thomas GM (2019) Identification of novel inhibitors of DLK palmitoylation and signaling by high content screening. *Sci Rep* 9: 3632
- Mata M, Merritt SE, Fan G, Yu GG, Holzman LB (1996) Characterization of dual leucine zipper-bearing kinase, a mixed lineage kinase present in synaptic terminals whose phosphorylation state is regulated by membrane depolarization via calcineurin. *J Biol Chem* 271: 16888–16896
- Mattson MP (2000) Apoptosis in neurodegenerative disorders. *Nat Rev Mol Cell Biol* 1: 120–130
- Mebratu YA, Dickey BF, Evans C, Tesfaigzi Y (2008) The BH3-only protein Bik|Blk|Nbk inhibits nuclear translocation of activated ERK1/2 to mediate IFN γ -induced cell death. *J Cell Biol* 183: 429–439
- Miller BR, Press C, Daniels RW, Sasaki Y, Milbrandt J, Diantonio A (2009) A dual leucine kinase-dependent axon self-destruction program promotes Wallerian degeneration. *Nat Neurosci* 12: 387–389
- Niu J, Holland SM, Ketschek A, Collura KM, Hesketh NL, Hayashi T, Gallo G, Thomas GM (2022) Palmitoylation couples the kinases DLK and JNK3 to facilitate prodegenerative axon-to-soma signaling. *Sci Signal* 15: eabh2674
- Patel S, Cohen F, Dean BJ, De La Torre K, Deshmukh G, Estrada AA, Ghosh AS, Gibbons P, Gustafson A, Huestis MP et al (2015) Discovery of dual leucine zipper kinase (DLK, MAP3K12) inhibitors with activity in neurodegeneration models. *J Med Chem* 58: 401–418
- Perslon E, Maday S, Fu M-M, Moughamian AJ, Holzbaur ELF (2010) Retrograde axonal transport: pathways to cell death? *Trends Neurosci* 33: 335–344

- Pistor S, Chakraborty T, Niebuhr K, Domann E, Wehland J (1994) The ActA protein of *Listeria monocytogenes* acts as a nucleator inducing reorganization of the actin cytoskeleton. *EMBO J* 13: 758–763
- Pozniak CD, Sengupta Ghosh A, Gogineni A, Hanson JE, Lee S-H, Larson JL, Solano H, Bustos D, Li H, Ngu H et al (2013) Dual leucine zipper kinase is required for excitotoxicity-induced neuronal degeneration. *J Exp Med* 210: 2553–2567
- Salaun C, Greaves J, Chamberlain LH (2010) The intracellular dynamic of protein palmitoylation. *J Cell Biol* 191: 1229–1238
- Sasaki Y, Vohra BPS, Lund FE, Milbrandt J (2009) Nicotinamide mononucleotide adenyl transferase-mediated axonal protection requires enzymatic activity but not increased levels of neuronal nicotinamide adenine dinucleotide. *J Neurosci* 29: 5525–5535
- Shin JE, Cho Y, Beirowski B, Milbrandt J, Cavalli V, DiAntonio A (2012) Dual leucine zipper kinase is required for retrograde injury signaling and axonal regeneration. *Neuron* 74: 1015–1022
- Stokoe D, Macdonald SG, Cadwallader K, Symons M, Hancock JF (1994) Activation of Raf as a result of recruitment to the plasma membrane. *Science* 264: 1463–1467
- Tedeschi A, Bradke F (2013) The DLK signalling pathway - A double-edged sword in neural development and regeneration. *EMBO Rep* 14: 605–614
- Teuling E, Ahmed S, Haasdijk E, Demmers J, Steinmetz MO, Akhmanova A, Jaarsma D, Hoogenraad CC (2007) Motor neuron disease-associated mutant vesicle-associated membrane protein-associated protein (VAP) B recruits wild-type VAPs into endoplasmic reticulum-derived tubular aggregates. *J Neurosci* 27: 9801–9815
- Tripathi P, Zhu Z, Qin H, Elsherbini A, Crivelli SM, Roush E, Wang G, Spassieva SD, Bieberich E (2021) Palmitoylation of acetylated tubulin and association with ceramide-rich platforms is critical for ciliogenesis. *J Lipid Res* 62: 100021
- Tulpule A, Guan J, Neel DS, Allegakoen HR, Lin YP, Brown D, Chou Y-T, Heslin A, Chatterjee N, Perati S et al (2021) Kinase-mediated RAS signaling via membraneless cytoplasmic protein granules. *Cell* 184: 2649–2664.e18
- Virdee K, Tolkovsky AM (1995) Activation of p44 and p42 MAP kinases is not essential for the survival of rat sympathetic neurons. *Eur J Neurosci* 7: 2159–2169
- Wainstein E, Seger R (2016) The dynamic subcellular localization of ERK: mechanisms of translocation and role in various organelles. *Curr Opin Cell Biol* 39: 15–20
- Watkins TA, Wang B, Huntwork-Rodriguez S, Yang J, Jiang Z, Eastham-Anderson J, Modrusan Z, Kaminker JS, Tessier-Lavigne M, Lewcock JW (2013) DLK initiates a transcriptional program that couples apoptotic and regenerative responses to axonal injury. *Proc Natl Acad Sci USA* 110: 4039–4044
- Welsbie DS, Mitchell KL, Jaskula-Ranga V, Sluch VM, Yang Z, Kim J, Buehler E, Patel A, Martin SE, Zhang P-W et al (2017) Enhanced functional genomic screening identifies novel mediators of dual leucine zipper kinase-dependent injury signaling in neurons. *Neuron* 94: 1142–1154.e6
- Welsbie DS, Yang Z, Ge Y, Mitchell KL, Zhou X, Martin SE, Berlinic CA, Hackler L, Fuller J, Fu J et al (2013) Functional genomic screening identifies dual leucine zipper kinase as a key mediator of retinal ganglion cell death. *Proc Natl Acad Sci USA* 110: 4045–4050
- Welsbie DS, Ziogas NK, Xu L, Kim BJ, Ge Y, Patel AK, Ryu J, Lehar M, Alexandris AS, Stewart N et al (2019) Targeted disruption of dual leucine zipper kinase and leucine zipper kinase promotes neuronal survival in a model of diffuse traumatic brain injury. *Mol Neurodegener* 14: 44
- Wessel D, Flügge UI (1984) A method for the quantitative recovery of protein in dilute solution in the presence of detergents and lipids. *Anal Biochem* 138: 141–143
- Witzel F, Maddison L, Blüthgen N (2012) How scaffolds shape MAPK signaling: what we know and opportunities for systems approaches. *Front Physiol* 3: 475
- Wlaschin JJ, Gluski JM, Nguyen E, Silberberg H, Thompson JH, Chesler AT, Le Pichon CE (2018) Dual leucine zipper Kinase is required for mechanical allodynia and microgliosis after nerve injury. *Elife* 7: 1–19
- Wu H (2013) Higher-order assemblies in a new paradigm of signal transduction. *Cell* 153: 287–292
- Xia Z, Dickens M, Raingeaud J, Davis RJ, Greenberg ME (1995) Opposing effects of ERK and JNK-p38 MAP kinases on apoptosis. *Science* 270: 1326–1331
- Xiong X, Lee CF, Li W, Yu J, Zhu L, Kim Y, Zhang H, Sun H (2019) Acid sphingomyelinase regulates the localization and trafficking of palmitoylated proteins. *Biol Open* 8: bio040311
- Xu Z, Maroney AC, Dobrzanski P, Kukekov NV, Greene LA (2001) The MLK family mediates c-Jun N-terminal kinase activation in neuronal apoptosis. *Mol Cell Biol* 21: 4713–4724
- Yamaguchi Y, Miura M (2015) Programmed cell death in neurodevelopment. *Dev Cell* 32: 478–490
- Yang G, Liu Y, Yang K, Liu R, Zhu S, Coquinco A, Wen W, Kojic L, Jia W, Cynader M (2012) Isoform-specific palmitoylation of JNK regulates axonal development. *Cell Death Differ* 19: 553–561
- Yang J, Wu Z, Renier N, Simon DJ, Uryu K, Park DS, Greer PA, Tournier C, Davis RJ, Tessier-Lavigne M (2015) Pathological axonal death through a Mapk cascade that triggers a local energy deficit. *Cell* 160: 161–176
- Yang Y, Lee M, Fairn GD (2018) Phospholipid subcellular localization and dynamics. *J Biol Chem* 293: 6230–6240
- Yarza R, Vela S, Solas M, Ramirez MJ (2016) c-Jun N-terminal kinase (JNK) signaling as a therapeutic target for Alzheimer's disease. *Front Pharmacol* 6: 321
- Zamzow DR, Elias V, Acosta VA, Escobedo E, Magnusson KR (2019) Higher levels of protein palmitoylation in the frontal cortex across aging were associated with reference memory and executive function declines. *eNeuro* 6: ENEURO.0310-18.2019
- Zareba-Kozioł M, Bartkowiak-Kaczmarek A, Figiel I, Krzystyniak A, Wojtowicz T, Bijata M, Włodarczyk J (2019) Stress-induced changes in the S-palmitoylation and S-nitrosylation of synaptic proteins. *Mol Cell Proteomics* 18: 1916–1938
- Zhang H, Cao X, Tang M, Zhong G, Si Y, Li H, Zhu F, Liao Q, Li L, Zhao J et al (2021) A subcellular map of the human kinome. *Elife* 10: e64943
- Zhang JZ, Lu T-W, Stolerman LM, Tenner B, Yang JR, Zhang J-F, Falcke M, Rangamani P, Taylor SS, Mehta S et al (2020) Phase separation of a PKA regulatory subunit controls cAMP compartmentation and oncogenic signaling. *Cell* 182: 1531–1544.e15



License: This is an open access article under the terms of the Creative Commons Attribution-NonCommercial-NoDerivs 4.0 License, which permits use and distribution in any medium, provided the original work is properly cited, the use is non-commercial and no modifications or adaptations are made.